Calculations of Axisymmetric Stability of Tokamak Plasmas with Active and Passive Feedback

D. J. WARD,* S. C. JARDIN, AND C. Z. CHENG

Plasma Physics Laboratory, Princeton University, Princeton, New Jersey 08543

A new linear MHD stability code, NOVA-W, has been developed in order to study feedback stabilization of the axisymmetric mode in deformable tokamak plasmas. The NOVA-W code is a modification of the non-variational MHD stability code NOVA that includes the effects of resistive passive conductors and active feedback circuits. The vacuum calculation has been reformulated in terms of the perturbed poloidal flux to allow the inclusion of perturbed toroidal currents outside the plasma. The boundary condition at the plasma–vacuum interface relates the instability displacement to the perturbed poloidal flux. This allows a solution of the linear MHD stability equations with the feedback effects included. The passive stability predictions of the code have been tested both against a simplified analytic model and against a different numerical calculation for a realistic tokamak configuration. The comparisons demonstrate the accuracy of the NOVA-W results. Active feedback calculations are performed for the CIT tokamak design demonstrating the effect of varying the position of the flux loops that provide the measurements of vertical displacement. The results compare well with those computed earlier using a less efficient nonlinear code. © 1993 Academic Press, Inc.

1. INTRODUCTION

It is now known that by increasing the total plasma current in a tokamak, one can increase both the maximum stable β [2] and the energy confinement time τ_E [3]. One way of increasing the total plasma current carrying capability of the tokamak without degrading the non-axisymmetric MHD stability is to modify the cross-sectional shape of the plasma by increasing its elongation and triangularity [4, 5]. Even further cross-sectional shaping such as indentation to produce a bean-shaped plasma may lead to even larger stable values of β by providing access to a second regime of stability against ballooning modes [6, 7].

Tokamak plasmas with strong cross-sectional shaping,

however, are subject to severe axisymmetric $(n = 0)$ instabilities that can destroy the plasma on the ideal MHD time scale [8–15]. The axisymmetric instability involves gross vertical plasma motion on the ideal MHD time scale. This results in the sudden termination of the tokamak discharge as the plasma comes into contact with the surrounding vacuum vessel structure. Such a disruption of the plasma discharge causes rapid quenching of the plasma current, which will induce large currents in the tokamak vacuum vessel and support structure, which will in turn produce large, potentially damaging forces.

These modes can be stabilized by placing a conducting wall around the plasma. The mode remains unstable when there is finite conductivity in the wall [16], but the growth rate is reduced from the ideal MHD time scale to the L/R time of the surrounding conductors [17, 18]. This time scale is much shorter than the length of the discharge in modern tokamak experiments but is long enough to be amenable to feedback stabilization using practical power supplies. Thus, an active feedback system is needed to further stabilize the plasma over the time of the discharge [19, 20].

The efficacy of the feedback control is highly dependent on the details of the active feedback system, the placement of the passive conductors, and the behavior of the plasma itself. In the past, the stabilizing properties of these feedback systems have been analyzed using simplified models that treat the plasma as a collection of filamentary currents, or as having purely rigid motion [20, 21]. Variational techniques have been used [22], but these still rely on the choice of a specified trial function, which might not be a good representation because plasmas with strong cross-sectional shaping can have large nonrigid components to their displacements [23]. In fact, it has been shown [24] that plasmas with strong cross-sectional shaping can remain unstable under the effects of a feedback system that would stabilize a plasma that undergoes only rigid motion.

The full nonlinear motion of a tokamak plasma can be simulated by a time-evolution code such as the Tokamak

* Present address: Centre de Recherches en Physique des Plasmas, Association Euratom-Confédération Suisse, École Polytechnique Fédérale de Lausanne, 21 av. des Bains, 1007 Lausanne, Switzerland.

Simulation Code (TSC) [25]. While TSC can provide an accurate treatment of both the linear and the nonlinear axisymmetric motion, obtaining an accurately converged result requires an excessive amount of computation. Thus to completely explore the performance of a feedback system using TSC is difficult and expensive. Also, the results of such simulations will not clearly demonstrate how the unstable motion of the plasma might deform with respect to variations in the feedback system.

Whereas analytical techniques have been used to find growth rates for axisymmetric modes in simple geometries with thin resistive walls [18, 22], a linear computational treatment capable of analyzing general geometries has not previously been available. One difficulty is that a realistic active feedback system will not satisfy the self-adjointness properties of the force operator. Therefore, ideal MHD stability codes such as PEST [26] or ERATO [27] cannot easily be modified to treat these non-ideal aspects, since that would destroy the self-adjointness property that is fundamental to their formulation. One is therefore limited to studying configurations with no feedback system and a perfectly conducting wall.

We describe here a *non*-ideal MHD stability code, NOVA-W, that calculates the linear stability of axisymmetric modes in general geometry with passive and active feedback included. To develop NOVA-W we have modified the vacuum calculation of the NOVA code [1] to include the effects of resistive conductors and feedback currents in the vacuum region. NOVA is non-variational MHD stability code that directly solves the stability eigenvalue equations without using the δW formulation. It can therefore be modified to include non-ideal effects that would otherwise destroy the self-adjointness property, which underlies the δW approach. The NOVA-W code is particularly well suited for examining the effects of active and passive feedback on the vertical instability in tokamaks with regard to the influence of the non-rigid components of the motion.

In the following section the formulation of the vacuum calculation is presented, as well as a review of the linear MHD stability equations that underlie the NOVA formulation. Resistive conductors in the vacuum region and an active feedback system are added to the formulation. In Section 3 the numerical method of the NOVA-W calculation is described for passive growth rates and active feedback stabilization. Section 4 presents results for passive stabilization studies. The code results are compared with an analytic model for a simplified configuration and with a different numerical calculation for a realistic tokamak equilibrium. The comparison is found to be excellent. In Section 5 we present results for an active feedback calculation. The results are found to compare well with results of a similar study performed using TSC [28]. Finally, in Section 6 we summarize our principal results.

2. FORMULATION

The NOVA stability code solves the linear MHD stability eigenvalue equations

$$\rho\omega^2\xi = \nabla p_1 + \mathbf{b} \times (\nabla \times \mathbf{B}) + \mathbf{B} \times (\nabla \times \mathbf{b}) \qquad (1)$$

$$p_1 + \xi \cdot \nabla P + \gamma P \nabla \cdot \xi = 0, \qquad (2)$$

where

$$\mathbf{b} = \nabla \times (\xi \times \mathbf{B}) \qquad (3)$$

is the perturbed magnetic field in the plasma, $\mathbf{B}$ is the equilibrium magnetic field, p_1 and P are the perturbed and equilibrium particle pressures, ρ is the plasma mass density, $\gamma = \frac{5}{3}$ is the ratio of specific heats, ξ is the displacement vector, and ω is the eigenvalue (normalized growth rate). The equations are solved directly, without using variational techniques. The equilibrium magnetic field is represented by

$$\mathbf{B} = \nabla \zeta \times \nabla \psi + q(\psi) \nabla \psi \times \nabla \Theta \qquad (4)$$

or

$$\mathbf{B} = \nabla \phi \times \nabla \psi + g(\psi) \nabla \phi, \qquad (5)$$

where $2\pi\psi$ is the poloidal flux contained within a surface, Θ is the generalized poloidal angle, ζ is the generalized toroidal angle, ϕ is the standard toroidal angle from (X, ϕ, Z) cylindrical coordinates, $q(\psi)$ is the safety factor, and $g(\psi)$ is the toroidal field function. The second definition for $\mathbf{B}$, Eq. (5), follows for an axisymmetric equilibrium. The generalized angle coordinates (Θ, ζ) are chosen to make the magnetic field lines appear straight in this coordinate system.

Equations (1)–(3) can be shown to reduce to a single matrix equation,

$$\nabla\psi \cdot \nabla \begin{pmatrix} P_1 \\ \xi_\psi \end{pmatrix} = \mathbf{C} \begin{pmatrix} P_1 \\ \xi_\psi \end{pmatrix} + \mathbf{D} \cdot \mathbf{E}^{-1} \cdot \mathbf{F} \begin{pmatrix} P_1 \\ \xi_\psi \end{pmatrix}, \qquad (6)$$

where P_1 is the total perturbed pressure, $P_1 = p_1 + \mathbf{b} \cdot \mathbf{B}$, and $\mathbf{C}$, $\mathbf{D}$, $\mathbf{E}$, and $\mathbf{F}$ are matrix operators involving surface derivatives $\mathbf{B} \cdot \nabla$ and $(\mathbf{B} \times \nabla\psi) \cdot \nabla$. These matrices are defined in the original NOVA paper [1].

This matrix equation (6) is essentially a pair of coupled first-order (in ψ) differential equations for ξ_ψ and P_1. In order for NOVA to solve this differential equation, the proper boundary condition at the plasma–vacuum interface must be provided. This boundary condition must relate P_1 to ξ_ψ at the boundary.

2.1. Poloidal Flux Formulation

We consider the geometry shown in Fig. 1. The plasma is surrounded by a vacuum region which is itself divided into two parts, Region I and Region II, by a thin resistive wall. Flux-loop sensors, poloidal magnetic field detectors, and active feedback coils may exist in either region. We are restricting consideration to axisymmetric modes. This enables us to use the axisymmetric flux formulation to represent the perturbed magnetic field in each vacuum region; thus

$$\mathbf{b} = \frac{1}{2\pi} \nabla \phi \times \nabla \chi + a_t \nabla \phi. \tag{7}$$

Here χ is the perturbed poloidal flux and a_t is related to the perturbed toroidal field.

The perturbed currents in the vacuum region are restricted to be the toroidal currents generated by the feedback system in the active feedback coils. Ampere's law therefore gives us

$$\nabla \times \mathbf{b} = \mu_0 j_{A.F.} \hat{\phi}, \tag{8}$$

where $\hat{\phi} = \nabla \phi / |\nabla \phi| = X \nabla \phi$ is a unit vector in the toroidal direction. From this and from Eq. (7), we find that

$$\frac{\partial a_t}{\partial \psi} = \frac{\partial a_t}{\partial \Theta} = 0. \tag{9}$$

Therefore a_t must be equal to a constant in each vacuum region.
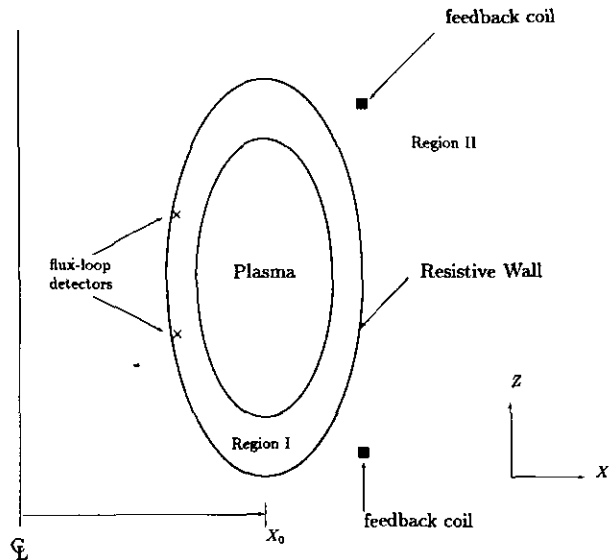

FIG. 1. Plasma and resistive wall, showing definitions of Regions I and II. The active feedback coils are outside the resistive wall in Region II. The flux-loop detectors are within the resistive wall in Region I (Case A derived in Section 2.3.1). They can also be placed in Region II (Case B derived in Section 1 of the Appendix).

The perturbed poloidal flux χ is related to the perturbed toroidal currents in the vacuum region:

$$X \nabla \cdot \left(\frac{1}{X^2} \nabla \chi \right) = 2\pi \mu_0 j_{A.F.}, \tag{10}$$

where we use the standard (X, ϕ, Z) cylindrical coordinates. The current density in the active feedback coils is represented by

$$j_{A.F.} = \sum_{i=1}^{N} I_m \delta(\mathbf{r} - \mathbf{r}_i). \tag{11}$$

Here, the I_m are the perturbed currents in axisymmetric coils that are part of an active feedback system in the vacuum region located at $\mathbf{r}_i = (X_i, Z_i)$. The sum is over all the feedback coils.

We solve Eq. (10) using Green's function techniques. The corresponding Green's function $G(\mathbf{r}_T; \mathbf{r}_S)$ is defined by

$$\nabla \cdot \frac{1}{X_T^2} \nabla G(X_T, Z_T; X_S, Z_S) = \frac{4\pi}{X_S} \delta(X_S - X_T) \delta(Z_S - Z_T). \tag{12}$$

The solution that vanishes at infinity is given by

$$G(\mathbf{r}_S; \mathbf{r}_T) = G(X_T, Z_T; X_S, Z_S) = 4\pi \frac{X_T X_S}{r} P_{1/2}^1(w),$$

where

$$w = X_S^2 + X_T^2 + (Z_S - Z_T)^2$$

$$r = [(X_S^2 - X_T^2)^2 + (Z_S - Z_T)^4 + 2(X_S^2 + X_T^2)(Z_S - Z_T)^2]$$

and where $P_{1/2}^1$ is the associated Legendre polynomial of order $\frac{1}{2}$ (also known as a toroidal function or ring function) which can be expressed in terms of complete elliptic integrals [29].

By integrating Eqs. (10) and (12) over the volume of each vacuum region, a Green's equation is found that relates the perturbed vacuum flux to the currents in the vacuum region and to an integral over the boundary surfaces. Thus when the observation point $\mathbf{r}$ is on the contour, and the principal part definition of the line integral is used, we have

$$\chi(\mathbf{r}) = \sum_{i=1}^{N} \mu_0 I_i G(\mathbf{r}; \mathbf{r}_i)$$

$$+ \sum_S \frac{1}{2\pi} \oint_S \frac{dl_S}{X_S} [\chi \nabla_n G(\mathbf{r}; \mathbf{r}_S) - G(\mathbf{r}; \mathbf{r}_S) \nabla_n \chi], \tag{13}$$

where $\nabla_n \chi$ is shorthand for $\hat{n} \cdot \nabla \chi$. We define the feedback coil currents as the feedback gain multiplied by some

measure of the vertical displacement of the plasma. Magnetics measurements are most often used, and in particular the flux difference between up–down symmetric points gives a simple measurement of vertical displacement. For a symmetric equilibrium that undergoes fairly rigid motion, this gives a good measurement of vertical displacement. Therefore the desired feedback coil currents are given by

$$I_m = \alpha_m [\chi(X_{o1}, Z_{o1}) - \chi(X_{o2}, Z_{o2})]$$
$$+ \beta_m [\dot{\chi}(X_{o1}, Z_{o1}) - \dot{\chi}(X_{o2}, Z_{o2})], \qquad (14)$$

where α_m is the proportional feedback gain, β_m is the derivative feedback gain, and $\dot{\chi}$ is the time derivative of the perturbed flux. However, any combination of magnetics measurements can be used to define the feedback currents. For example, poloidal magnetic field measurements are sometimes also included as part of the signal for the feedback system [30]. Components of the perturbed magnetic field can be included in the feedback law, Eq. (14), by substituting Eq. (13) into Eq. (7).

The integrals in Eq. (13) are over the surfaces that are the boundaries to the vacuum region, i.e., the plasma–vacuum surface and the surface of the resistive wall surrounding the plasma. We take the principal part of the integral over the contour that is the interface or wall for a poloidal cross section of the torus. The incremental arc length dl on the contour is given by

$$dl = \frac{\mathscr{J} |\nabla \psi|}{X} d\Theta, \qquad (15)$$

where the Jacobian $\mathscr{J}$ is defined by

$$\mathscr{J}^{-1} = \nabla \psi \times \nabla \Theta \cdot \nabla \zeta. \qquad (16)$$

Separate Green's equations are obtained for vacuum Region I (between the plasma and the resistive wall—see Fig. 1), and for Region II (outside the resistive wall). By discretizing the quantities on the surface into a finite grid, the contour integrals in Eq. (13) are expressed as sums over the grid points on the surface. The collocation method [31] is used to solve the integral equations. Equation (13) is written M_Θ times, where M_Θ is the number of grid points on the plasma surface and wall surface, with every grid point on the surface serving once as the observation point $\mathbf{r} = (X, Z)$. This series of equations can be combined into a single matrix equation in which the integrals are expressed as matrices multiplying column vectors χ_p, $\nabla_n \chi_p$, χ_w, and $\nabla_n \chi_w$, which contain the values of the perturbed flux and its normal derivative at every collocation point on the plasma surface and wall surface, respectively. A total of three matrix equations result, corresponding to the number of surfaces

that are boundaries to the two regions. The Green's equations in matrix form for a configuration with feedback coils present in Region II, outside the resistive wall, are

$$(1 + \mathbf{M}_{pp}) \cdot \chi_p + \mathbf{M}_{pw} \cdot \chi_w$$
$$= \mathbf{G}_{pp} \cdot \nabla_n \chi_p + \mathbf{G}_{pw} \cdot \nabla_n \chi_w, \qquad (17)$$

$$\mathbf{M}_{wp} \cdot \chi_p + (1 + \mathbf{M}_{ww}) \cdot \chi_w$$
$$= \mathbf{G}_{wp} \cdot \nabla_n \chi_p + \mathbf{G}_{ww} \cdot \nabla_n \chi_w, \qquad (18)$$

$$(1 + \mathbf{M}_{ww}^+) \cdot \chi_w^+$$
$$= \mathbf{G}_{ww}^+ \cdot \nabla_n \chi_w^+ + \mathbf{P}_w \cdot \chi_w$$
$$+ \mathbf{N}_w \cdot \nabla_n \chi_w + \mathbf{P}_p \cdot \chi_p + \mathbf{N}_p \cdot \nabla_n \chi_p. \qquad (19)$$

Here the matrices $\mathbf{M}$ and $\mathbf{G}$ are defined such that the ith components of the matrix–vector products are given by

$$\mathbf{M}_{wp}^i \cdot \chi_p = -\frac{1}{2\pi} \oint_p \frac{dl_p}{X_p} (\hat{\mathbf{n}} \cdot \nabla G(\mathbf{r}_p; \mathbf{r}_w^i)) \chi(\mathbf{r}_p), \qquad (20)$$

$$\mathbf{G}_{pw}^i \cdot \nabla_n \chi_w = -\frac{1}{2\pi} \oint_w \frac{dl_w}{X_w} G(\mathbf{r}_w; \mathbf{r}_p^i)(\hat{\mathbf{n}} \cdot \nabla \chi(\mathbf{r}_w)), \qquad (21)$$

and so on, with the definitions for the other matrices following the subscripts. The identity matrix is expressed by $\mathbf{1}$, and the normal vector is defined by $\hat{\mathbf{n}} = \nabla \psi / |\nabla \psi|$. Also, $\mathbf{r}_p^i$ is the ith point on the plasma–vacuum surface, and $\mathbf{r}_w^i$ is the ith point of the wall. The "+" superscripts denote quantities on the outer surface of the thin resistive wall (Region II). The w subscript without the "+" superscript denotes the inner surface of the wall (Region I), and the p subscript denotes the plasma surface. The integrals are over the plasma or wall contours. The matrix Green's equations (17)–(18) are the Green's equations for Region I. The final equation, Eq. (19), is that for Region II.

By using the thin–wall approximation, we get an expression that relates the jump in the normal derivative across the thin resistive wall boundary to the time derivative of the flux on the boundary,

$$[\![(\hat{\mathbf{n}} \cdot \nabla \chi)]\!] = -i\omega \mu_0 \frac{\delta}{\eta} \chi_w = K \chi_w, \qquad (22)$$

where $[\![\ ]\!]$ denotes the jump across the thin resistive wall, δ is the thickness, and η is the resistivity of the wall. This relation can be derived directly from Maxwell's equations, and it can also be found by taking the Green's equation for the resistive wall region in the limit as the wall thickness goes to zero. By using a variable jump coefficient $K(\Theta)$ at the various theta points we can simulate a wall with variable thickness and material resistivity, and even a wall with toroidally axisymmetric gaps. The thin-wall approximation also implies that the poloidal flux is continuous across the wall: $\chi_w^+ = \chi_w$.

The matrices $\mathbf{P}$ and $\mathbf{N}$ contain the effects of the active feedback system. The forms of the feedback matrices $\mathbf{P}$ and $\mathbf{N}$ are quite different depending on whether the observation flux loops controlling the feedback system are in Region I or Region II (see Fig. 1). Since the active feedback currents are a linear function of the perturbed flux at the observation points, they can, after some algebra, be expressed in terms of matrix relations involving χ and $\nabla_n \chi$ on the wall and plasma surfaces.

Consider the case with a resistive wall and no active feedback system, so that the matrices $\mathbf{P}$ and $\mathbf{N}$ in Eq. (19) vanish. Equations (17)–(19) may be solved to obtain $\nabla_n \chi_p$ in terms of χ_p. First χ_w is eliminated in favor of $\nabla_n \chi_w$ in Eq. (19), using Eq. (22). Then from Eq. (18) $\nabla_n \chi_w$ is calculated in terms of χ_p and $\nabla_n \chi_p$. Finally Eq. (17) gives $\nabla_n \chi_p$ in terms of χ_p. Therefore we find that

$$\nabla_n \chi_p = \mathbf{E}^{-1} \cdot \mathbf{D} \cdot \chi_p, \tag{23}$$

where

$$\begin{aligned}
\mathbf{E} &= \mathbf{G}_{pp} - \mathbf{C} \cdot \mathbf{B}^{-1} \cdot \mathbf{G}_{wp} \\
\mathbf{D} &= (1 + \mathbf{M}_{pp}) - \mathbf{C} \cdot \mathbf{B}^{-1} \cdot \mathbf{M}_{wp} \\
\mathbf{C} &= \mathbf{G}_{pw} + \mathbf{M}_{pw} \cdot \mathbf{A}^{-1} \cdot \mathbf{G}_{ww} \\
\mathbf{B} &= \mathbf{G}_{ww} + (1 + \mathbf{M}_{ww}) \cdot \mathbf{A}^{-1} \cdot \mathbf{G}_{ww} \\
\mathbf{A} &= (1 - \mathbf{M}_{ww} + K \mathbf{G}_{ww}).
\end{aligned} \tag{24}$$

For the case with active feedback the procedure is essentially the same, but then the feedback matrices must be included in the definitions for matrices $\mathbf{A}$ through $\mathbf{D}$.

2.2. Boundary Conditions at the Plasma–Vacuum Interface

The necessary boundary condition for Eq. (6) requires that we provide P_1 in terms of ξ_ψ at the plasma–vacuum boundary. The perturbed pressure P_1 at the plasma–vacuum interface is found in terms of the normal derivative of the flux at the boundary,

$$\begin{aligned}
P_1 &= \mathbf{B} \cdot \mathbf{b} = (\nabla\phi \times \nabla\psi) \cdot \left(\nabla\phi \times \frac{\nabla\chi}{2\pi}\right) + g(\psi_{\text{edge}}) \nabla\phi \cdot a_t \nabla\phi \\
&= \frac{|\nabla\psi|}{2\pi X^2} \nabla_n \chi + a_t g(\psi_{\text{edge}}) \frac{1}{X^2},
\end{aligned} \tag{25}$$

where ψ_{edge} is the value of ψ at the plasma–vacuum boundary.

In order to evaluate this expression for P_1 in terms of ξ_ψ we relate the perturbed vacuum magnetic field to the plasma perturbed field at the interface. Recall Eq. (7):

$$\mathbf{b} = \frac{1}{2\pi} \nabla\phi \times \nabla\chi + a_t \nabla\phi.$$

Since $\mathbf{b} = \nabla \times \delta\mathbf{A}$ we can find $\delta\mathbf{A}$,

$$\delta\mathbf{A} = -\frac{1}{2\pi} \chi \nabla\phi + a_t \ln X \left[\frac{\partial Z}{\partial\psi}\nabla\psi + \frac{\partial Z}{\partial\Theta}\nabla\Theta\right] + \nabla F, \tag{26}$$

where F is some arbitrary scalar function. From Eq. (3) we can compute the form of $\delta\mathbf{A}$ on the plasma surface:

$$\delta\mathbf{A} = \xi \times \mathbf{B}. \tag{27}$$

Equating Eqs. (26) and (27) and taking the projection along $\nabla\phi$, we find

$$\nabla\phi \cdot \xi \times \mathbf{B} = -\frac{1}{2\pi} \chi |\nabla\phi|^2 \tag{28}$$

or

$$\xi_\psi = \xi \cdot \nabla\psi = \sum_m \xi_m \exp(im\Theta) = -\frac{1}{2\pi} \chi. \tag{29}$$

This, together with Eq. (23), gives the required relation between the normal derivative of the perturbed poloidal flux $\nabla_n \chi$ at the interface and the Fourier modes of the displacement ξ_m. Therefore we need calculate only the toroidal perturbation a_t to complete the vacuum calculation.

To find a_t, we first substitute the definition for $\mathbf{b}$ in the vacuum, Eq. (7), into Faraday's law, then take the toroidal projection of this equation and integrate over the surface defined by a plane at constant ϕ between the plasma and the conducting wall. This gives

$$-i\omega \oint \frac{a_t}{X} dS = -\oint_w \delta\mathbf{E} \cdot d\mathbf{l} - \oint_p \delta\mathbf{E} \cdot d\mathbf{l} \tag{30}$$

or

$$L_w \frac{\partial I_w}{\partial t} + R_w I_w = (R_w - i\omega L_w) I_w = -\oint_p \delta\mathbf{E} \cdot d\mathbf{l}, \tag{31}$$

where $I_w \equiv 2\pi a_t/\mu_0$ is the poloidal current induced in the surrounding wall owing to the toroidal part of the magnetic field perturbation $\mathbf{b}$, $L_w \equiv \mu_0 \int dS/2\pi X$ is the corresponding self-inductance term, R_w is the poloidal resistance of the resistive wall.

We determine I_w, and hence a_t, from this "circuit" equation. We evaluate the integral on the right-hand side of Eq. (31), using Eqs. (5), (27), and (29), thus

$$\begin{aligned}
-\oint_p \delta\mathbf{E} \cdot d\mathbf{l} &= i\omega \oint_p (\xi \times \mathbf{B}) \cdot \hat{t}\, dl \\
&= -i\omega g(\psi_{\text{edge}}) \sum_m \xi_m \oint_p \frac{\mathscr{J}}{X^2} \exp(im\Theta)\, d\Theta.
\end{aligned} \tag{32}$$

where $\hat{t}$ is the surface unit tangent vector $\hat{t} = \hat{\phi} \times \hat{n}$.

It is interesting to note that if one is using PEST [26] coordinates ($\mathscr{J} = X^2$), then only the $m = 0$ term will contribute to the sum (corresponding to a pure compression of the plasma cross section). Completing the circuit equation (31) and solving for I_w yields an expression for a_t,

$$a_t = \frac{-i\omega\mu_0 \, g(\psi_{edge})}{2\pi(R_w - i\omega L_w)} \sum_m \xi_m \int_0^{2\pi} \frac{\mathscr{J}}{X^2} \exp(im\Theta) \, d\Theta, \quad (33)$$

where the poloidal resistance R_w is given by Ohm's law to be

$$R_w = \oint_w \frac{\eta}{\delta} \frac{dl}{2\pi X}. \quad (34)$$

It is also interesting to note that the result we obtain for a_t in Eq. (33) in the limit of a perfectly conducting wall ($R_w = 0$) is the same result obtained using the method of Lüst and Martenson [32]. The expression that we derive for the resistive wall using the circuit model in fact differs from the expression of the ideal wall of Lüst and Martenson only by a factor of $-i\omega L_w/(R_w - i\omega L_w)$.

Finally, we perform a Fourier integral of the expression in Eq. (25) to get P_1 in terms of the Fourier modes:

$$P_1 = \mathbf{b} \cdot \mathbf{B} = \sum_m p_m \exp(im\Theta) = \sum_{m,m'} \tilde{\mathbf{M}}_{m,m'} \xi_{m'} \exp(im\Theta). \quad (35)$$

The matrix $\tilde{\mathbf{M}}$ is the final result of the vacuum calculation. This matrix relates P_1 at the boundary to the Fourier coefficients of ξ_ψ and includes the effects of the resistive conductors, the active feedback currents, and the geometry of the vacuum region.

2.3. Active Feedback Matrices

Here we derive the form of the feedback matrices $\mathbf{P}$ and $\mathbf{N}$ in Eq. (19) given the simple feedback law of Eq. (14). As mentioned above, the form of the feedback matrices depends on the region in which the flux observation detection loops are located. We begin with the basic Green's equation defining the perturbed poloidal flux at an observation point $\mathbf{r}_o = (X_o, Z_o)$ not on the plasma surface or the wall surface. The analogue of Eq. (13) for this case is

$$\chi(\mathbf{r}_o) = \frac{1}{2} \sum_{m=1}^{M} \mu_0 I_m G(\mathbf{r}_m; \mathbf{r}_o)$$
$$+ \frac{1}{4\pi} \oint \frac{dl_T}{X_T} \chi_T (\hat{n} \cdot \nabla_T G(\mathbf{r}_T; \mathbf{r}_o))$$
$$- \frac{1}{4\pi} \oint \frac{dl_T}{X_T} G(\mathbf{r}_T; \mathbf{r}_o)(\hat{n} \cdot \nabla_T \chi_T). \quad (36)$$

The magnitudes of the feedback coil currents are proportional to the difference between the perturbed poloidal fluxes at the two observation points as given in Eq. (14). Therefore we must calculate the value of the perturbed flux χ at these points in terms of surface integrals over χ and $\nabla_n\chi$ from Eq. (36). Here we see that the form of the feedback matrices depends upon the region in which the flux-loop detectors are located. The value of the perturbed flux at some point in Region I, as calculated from Eq. (36), will clearly depend on integrals over the surface of the plasma as well as the inner surface of the resistive wall. On the other hand, if the detectors are in Region II, the value of χ at the observation points will depend on the surface integrals only over the outer surface of the wall. In addition, however, there will be a direct contribution from the feedback coils themselves, as opposed to the former case, in which the detectors in Region I "feel" the active feedback coils only through the boundary condition that connects Region I and Region II.

In this section we consider only current-control feedback, in which the actual feedback currents are proportional to the difference of the flux-loop measurements and their time derivatives. The currents are axisymmetric current loops which do not obey any circuit equations. The formulation for the case of voltage feedback, in which the circuit equations of the active feedback coils are included in the feedback matrices, will be presented in Section 2 of the Appendix.

2.3.1. Case A: Detector Loops in Region I

We consider first the case in which the observation points are located in Region I, while the active feedback coils are in Region II. We use Eq. (36) to evaluate the perturbed flux at the observation points. The region is bounded by the plasma surface and the wall surface; therefore the flux at the observation point $\mathbf{r}_{o1} = (X_{o1}, Z_{o1})$ is given by

$$\chi(\mathbf{r}_{o1}) = -\mathbf{M}_{o1,p} \cdot \chi_p - \mathbf{M}_{o1,w} \cdot \chi_w$$
$$+ \mathbf{G}_{o1,p} \cdot \nabla_n\chi_p + \mathbf{G}_{o1,w} \cdot \nabla_n\chi_w, \quad (37)$$

where

$$\mathbf{M}_{o1,w} \cdot \chi_w = -\frac{1}{4\pi} \oint_w \frac{dl_w}{X_w} (\hat{n} \cdot \nabla G(\mathbf{r}_w; \mathbf{r}_{o1})) \chi(\mathbf{r}_w)$$
$$(38)$$
$$\mathbf{G}_{o1,w} \cdot \nabla_n\chi_w = -\frac{1}{4\pi} \oint_w \frac{dl_w}{X_w} G(\mathbf{r}_w; \mathbf{r}_{o1})(\hat{n} \cdot \nabla\chi(\mathbf{r}_w))$$

and similarly for $\mathbf{G}_{o1,p} \cdot \nabla_n\chi_p$ and $\mathbf{M}_{o1,p} \cdot \chi_p$. Note that the arrays $\mathbf{G}_{o1,p}, \mathbf{M}_{o1,p}, ...$ are row vectors, as opposed to matrices as in the case of $\mathbf{M}_{pp}, \mathbf{G}_{wp}, ...$ from the previous

section, because we are evaluating χ on the left-hand side of Eq. (36) at only one observation point at a time, instead of over all points of the plasma surface or wall surface grid. The equivalent equation gives the flux $\chi(\mathbf{r}_{o2})$ at the observation point $\mathbf{r}_{o2} = (X_{o2}, Z_{o2})$.

We combine Eq. (37) with Eq. (14) to give the desired currents in the active feedback coils:

$$
\begin{aligned}
I_m &= \alpha_m(\chi(\mathbf{r}_{o1}) - \chi(\mathbf{r}_{o2})) + \beta_m(\dot\chi(\mathbf{r}_{o1}) - \dot\chi(\mathbf{r}_{o2})) \\
&= (\alpha_m - i\omega\beta_m)(\chi(\mathbf{r}_{o1}) - \chi(\mathbf{r}_{o2})) \\
&= (\alpha_m - i\omega\beta_m)\{ -\mathbf{M}_{o1,p} \cdot \chi_p - \mathbf{M}_{o1,w} \cdot \chi_w \\
&\quad + \mathbf{M}_{o2,p} \cdot \chi_p + \mathbf{M}_{o2,w} \cdot \chi_w + \mathbf{G}_{o1,p} \cdot \nabla_n\chi_p \\
&\quad + \mathbf{G}_{o1,w} \cdot \nabla_n\chi_w - \mathbf{G}_{o2,p} \cdot \nabla_n\chi_p - \mathbf{G}_{o2,w} \cdot \nabla_n\chi_w \}.
\end{aligned}
\tag{39}
$$

Now we include this expression in the sum over the feedback coils in Eq. (13). Since the Green's function in the summation is evaluated at every grid point on the wall surface in order to derive the matrix equation (19), our feedback sum becomes a matrix in which the rows span the grid points on the wall. The elements (k, l) of $\mathbf{P}_w$ are defined by

$$
\mathbf{P}_w^{k,l} = -\sum_m (\alpha_m - i\omega\beta_m) G(\mathbf{r}_w^k; \mathbf{r}_c^m)[\mathbf{M}_{o1,w}^l - \mathbf{M}_{o2,w}^l].
\tag{40}
$$

The summation here is over all the active feedback coils; $\mathbf{r}_c^m$ is the position of the mth feedback coil, and $\mathbf{r}_w^k$ is the position of the kth grid point on the wall surface. Each coil may have a different set of gain coefficients (α_m, β_m) and there may be any number of coils. This will not affect the size of the feedback matrix, as its row and column dimensions are defined by the number of grid points on the wall surface or the plasma surface. The elements (k, l) of $\mathbf{N}_w$, $\mathbf{P}_p$, and $\mathbf{N}_p$, are given by

$$
\mathbf{N}_w^{k,l} = \sum_m (\alpha_m - i\omega\beta_m) G(\mathbf{r}_w^k; \mathbf{r}_c^m)[\mathbf{G}_{o1,w}^l - \mathbf{G}_{o2,w}^l],
\tag{41}
$$

$$
\mathbf{P}_p^{k,l} = -\sum_m (\alpha_m - i\omega\beta_m) G(\mathbf{r}_w^k; \mathbf{r}_c^m)[\mathbf{M}_{o1,p}^l - \mathbf{M}_{o2,p}^l],
\tag{42}
$$

$$
\mathbf{N}_p^{k,l} = \sum_m (\alpha_m - i\omega\beta_m) G(\mathbf{r}_w^k; \mathbf{r}_c^m)[\mathbf{G}_{o1,p}^l - \mathbf{G}_{o2,p}^l].
\tag{43}
$$

The matrix equations to be solved are now in the form of Eqs. (17)–(19), with the active feedback matrices nonzero. We can now rewrite Eq. (23) to include the feedback matrices. Now, however, the equation is a bit more complicated;

$$
\nabla_n\chi_p = \mathbf{E}^{-1} \cdot \mathbf{D} \cdot \chi_p,
\tag{44}
$$

where

$$
\begin{aligned}
\mathbf{E} &= \mathbf{G}_{pp} - \mathbf{C} \cdot \mathbf{B}^{-1} \cdot \mathbf{G}_{wp} \\
&\quad - [\mathbf{M}_{pw} - \mathbf{C} \cdot \mathbf{B}^{-1} \cdot (1 + \mathbf{M}_{ww})] \cdot \mathbf{A}^{-1} \cdot \mathbf{N}_p \\
\mathbf{D} &= (1 + \mathbf{M}_{pp}) - \mathbf{C} \cdot \mathbf{B}^{-1} \cdot \mathbf{M}_{wp} \\
&\quad + [\mathbf{M}_{pw} - \mathbf{C} \cdot \mathbf{B}^{-1} \cdot (1 + \mathbf{M}_{ww})] \cdot \mathbf{A}^{-1} \cdot \mathbf{P}_p \quad (45) \\
\mathbf{C} &= \mathbf{G}_{pw} + \mathbf{M}_{pw} \cdot \mathbf{A}^{-1} \cdot (\mathbf{G}_{ww} - \mathbf{N}_w) \\
\mathbf{B} &= \mathbf{G}_{ww} + (1 + \mathbf{M}_{ww}) \cdot \mathbf{A}^{-1} \cdot (\mathbf{G}_{ww} - \mathbf{N}_w) \\
\mathbf{A} &= (1 - \mathbf{M}_{ww} + K\mathbf{G}_{ww} - \mathbf{P}_w).
\end{aligned}
$$

The additional complexity compared to the case with no feedback in Eq. (23) arises because of the additional matrices $\mathbf{P}$ and $\mathbf{N}$, and also because we have new terms that multiply χ_p and $\nabla_n\chi_p$, which appear in the *third* matrix equation (19). Previously, of course, these terms appeared only in the first two matrix equations, Eqs. (17)–(18). It is clear, however, that Eqs. (44)–(45) reduce to Eqs. (23)–(24) in the limit of zero feedback.

This formulation corresponds to the configuration in which the flux-loop detectors are inside the resistive wall (i.e., Region I, see Fig. 1). This is the configuration used in the calculations presented in Section 4. The feedback matrices for a feedback system that includes components of the poloidal magnetic field in the feedback law, Eq. (14), are derived in the same fashion as the above formulation by taking derivatives of Eq. (36), following Eq. (7). We will not give this derivation here. The formulation for the case of the flux-loop detectors exterior to the resistive wall (Case B) is given in the Section 1 of the Appendix. All the cases presented here assume that the active feedback coils are in Region II exterior to the resistive wall. The formulation for the unusual case of active feedback coils inside the resistive wall involves only a modification of the cases presented in this paper and will not be given here.

3. NUMERICAL METHOD

In this section we describe the method of calculating the growth rates of the axisymmetric mode for a realistic tokamak equilibrium with passive and active feedback. One begins with a 2D equilibrium code (free-boundary or fixed-boundary) that generates an equilibrium file compatible with the PEST [26] format. In principle, any equilibrium code can be used to generate the equilibria, but for the calculations presented in this article using realistic tokamak designs, the TSC [25] is used. The TSC calculates the free-boundary MHD equilibrium and transport for realistic tokamak configurations and can itself simulate the axi-symmetric motion of a vertically unstable plasma. The basic equilibrium information (profiles and plasma surface defini-

tion) provided by the TSC code is then used as input to a 2D fixed-boundary equilibrium code that calculates the axisymmetric MHD equilibrium to the desired accuracy.

The accurately resolved equilibrium is then mapped into a straight-magnetic-field-line stability coordinate system. Special care must be given to equilibria with x-points. Since the gradient of the poloidal flux vanishes at the x-point, the Jacobian is singular and the coordinate transformation becomes ill-defined. Therefore, defining the plasma–vacuum equilibrium boundary too close to the separatrix surface can adversely affect the accuracy of the mapping to stability coordinates and thereby affect the entire calculation. It should be noted here that the vacuum calculation depends on the metric quantities at the plasma surface; therefore these quantities must be well resolved on and near the surface. In practice, this is verified by performing convergence studies and verifying that the metric quantities at the plasma edge approach unique values as the number of grid points used in the equilibrium and mapping becomes large.

To obtain growth rates for equilibria with x-points we must extrapolate results from a family of equilibria, each limited by a surface successively closer to the separatrix. The boundary surface for each equilibrium in the sequence is labeled by the parameter ψ_{rat}, which is defined as the ratio of the poloidal flux contained within the given surface to the poloidal flux contained within the separatrix surface. Thus, $\psi_{rat} = 1.0$ labels the separatrix surface. For equilibria whose boundary surface is close to the separatrix ($\psi_{rat} \geqslant 0.97$) one must find the correct growth rate by performing a convergence study in the number of surfaces used in the equilibrium calculation. The shape of the boundary surface changes rapidly as ψ_{rat} approaches 1, and more equilibrium surfaces are needed to properly resolve the equilibrium. It is seen that the growth rates as a function of ψ_{rat} (near $\psi_{rat} = 1$) fit a straight line (see Fig. 5), which gives us a converged growth rate by extrapolating to $\psi_{rat} = 1$. It is more efficient to use equilibria in the range $0.94 \leqslant \psi_{rat} \leqslant 0.96$ to calculate the growth rate convergence, since it is much easier to obtain the converged growth rate of these individual equilibria. This is slightly less accurate than carrying out the convergence through to $\psi_{rat} = 0.99$, but it is much less time consuming, and the resulting growth rate is found to be within 5% of the properly converged growth rate.

The NOVA input code takes the equilibrium mapped into stability coordinates and evaluates the matrices, such as those in Eq. (6), needed by the eigenvalue solver. Then the NOVA-W code itself is executed; it performs the vacuum region calculation, including the feedback system and resistive conductors, and solves for the resulting eigenvalues of the linear MHD stability equations. The vacuum calculation must be performed at every iteration when searching for the root ω of the dispersion relation, since the boundary condition, Eq. (35), is a function of ω (see, for

example, Eq. (22)). The calculation for the case of an ideal vacuum region (i.e., with no wall or with an ideally conducting wall, and with no active feedback system) differs in that the vacuum boundary condition does not depend on ω (because the system is then self-adjoint), and therefore it needs to be calculated only once prior to the eigenvalue search.

3.1. Calculation of Passive Growth Rates

The NOVA code calculates an eigenvalue (growth rate) that is normalized to the poloidal Alfvén time. Therefore to find the actual growth rate we must include the normalization factor, given by

$$\gamma_0 = \frac{B_T(0)}{q(1) X_{mag}(\mu_0 \rho_0)^{1/2}}, \tag{46}$$

where $B_T(0)$ is the toroidal magnetic field strength at the magnetic axis, $q(1)$ is the safety factor at the plasma edge, X_{mag} is the major radius of the axis, and ρ_0 is the mass density at the magnetic axis. This normalization enters into Eq. (22), where the correct frequency, ω in s^{-1}, is needed for the jump condition. It also enters into the feedback current definition when there is a derivative gain term as in Eq. (14). For a configuration stable on the ideal MHD time scale, the growth time is nearly proportional to the resistivity, but influenced by the geometry of the plasma and wall. Therefore the surface integrals over the jump condition, Eq. (22), ultimately determine the growth rate of the instability. In this case, the accuracy of the normalization is not important, since the normalization factor is effectively canceled out of the calculation. However, when the wall is distant from the plasma and the plasma is approaching ideal instability (instability with a perfectly conducting wall), the correct normalization is important, since the growth rate is now affected by plasma inertia, and the mass density factor ρ_0 would then be an important part of the calculation.

3.2. Active Feedback Calculations

For the case of a wall-stabilized plasma in the presence of passive resistive conductors, we find that the solution of interest has a purely imaginary eigenvalue that corresponds to exponential growth of the instability on the resistive time scale of the surrounding conductors. This root does not exist in the absence of resistivity. With a perfectly conducting wall that stabilizes the ideal instability, there are two roots that are purely real (oscillatory). With the addition of resistivity these roots remain oscillatory but become damped, and a third root, the unstable root of interest, arises from the origin and moves along the imaginary axis. (A good discussion of resistive wall roots is given by Freidberg [33].) The addition of active feedback to the stability calculation is a non-ideal effect, destroying the self-adjointness of the stability equations. With the addition of

feedback, therefore, we cannot expect this root to remain purely imaginary.

The procedure for the calculation of stability with active feedback begins with the determination of the eigenvalues of the system with the feedback gain set to zero, as described in Section 3.1. One then increases the feedback gain from zero and tracks the motion of the eigenvalue in the complex plane. The eigenvalue is calculated using Muller's method (see, for example, Ref. [34]), for determining complex zeros of analytic functions in the complex plane. Since Muller's method assumes that the function is a smoothly varying function of ω and that one begins with a good initial guess, it works most reliably when we increment the gain in relatively small steps, so that the initial guess is relatively close to the actual solution. In practice the dispersion function $D(\omega)$ (resulting from Eq. (6) after being decomposed into poloidal harmonics and finite elements) is often a well-behaved and smoothly varying function for this problem, and therefore one can often make reasonably large increments of gain and successfully find the root, even with a poor initial guess. However, this is not always the case.

In many active feedback cases a real part to the eigenvalue develops. This corresponds to some oscillation in the vertical motion that can be detrimental to the effectiveness of the feedback system. Even if the imaginary part of the eigenvalue is negative (stable), a large real (oscillatory) piece indicates poor control. This oscillation can usually be reduced by introducing or increasing the derivative gain β_g in the gain law for the feedback currents:

$$I_{fb} = \alpha_g(\chi_{o1} - \chi_{o2}) + \beta_g(\dot{\chi}_{o1} - \dot{\chi}_{o2}). \qquad (47)$$

The oscillation is due to an "overshoot" in the plasma motion. In a linear system, if the slope of the response curve to a step input is large, a large overshoot will be the result [35]. The feedback system pulls strongly, trying to bring the vertical position to the desired value. The motion goes beyond the desired point, and the feedback reverses to try to bring it back. An oscillatory motion about the desired position is the result, which may be damped (stable) or growing. The derivative term measures the instantaneous slope and predicts and corrects for the overshoot before it happens. In Section 5 we shall see an example of a configuration with large oscillations in the feedback response and how increasing the derivative gain improves the feedback control.

4. PASSIVE STABILIZATION RESULTS

4.1. Code Test: Analytic Model

4.1.1. Dobrott and Chang Model

In this section we introduce an analytic model derived by Dobrott and Chang [18] that calculates growth rates of the vertical instability for a simplified plasma model with a resistive wall and discrete resistive conductors surrounding the plasma. The model uses a straight, constant-current-density plasma equilibrium with a simple elliptical cross section. This plasma model was first examined with regard to axisymmetric instability without any wall or conductors in the vacuum region by Rutherford [8]. Dobrott and Chang added to the model a thin resistive wall and discrete conductors that satisfy certain geometric constraints and derived a dispersion relation for the growth rate of the instability that is partially stabilized by the resistive wall. We will use the model with a thin resistive wall, but without any additional conductors in the vacuum region; this simplifies the results somewhat. We then compare results from a numerical approximation of this simplified model to the results predicted by the dispersion relation.

Dobrott and Chang derive a dispersion relation for the growth rate of the $m = 1$ mode,

$$\Omega^2 - \frac{b^2}{a^2} + \frac{b}{a}\frac{N_1(\sigma_w, \Omega)}{D_1(\sigma_w, \Omega)} = 0, \qquad (48)$$

where Ω is the growth rate normalized to a geometrically normalized Alfvén frequency. The numerator $N_1(\sigma_w, \Omega)$ and denominator $D_1(\sigma_w, \Omega)$ are functions of the normalized frequency Ω, the normalized wall conductivity σ_w, and the separation between the plasma and wall. The major and minor radii of the ellipse are given by b and a.

When there is no wall in the region surrounding the plasma, the normalized growth rate reduces to

$$\Omega_{nw} = \pm\left[\frac{b}{a}\left(\frac{b}{a} - 1\right)\right]^{1/2}. \qquad (49)$$

When the resistive wall is present one must solve Eq. (48) to obtain the resistive growth rates. The resulting cubic equation is a function of the wall conductivity σ_w and the wall separation from the plasma Δ_{wo}, as well as the elongation ratio b/a. The three roots correspond to the resistive wall roots [33]. We are interested only in the purely imaginary root.

4.1.2. Comparison of Numerical Results to Analytic Model

We approximate the constant-current-density straight elliptical plasma equilibrium of the analytic model by generating a numerical equilibrium of elliptical cross section with a very large aspect ratio ($A = 100$) and with a nearly constant current density. The q-profile for this numerical equilibrium increases from $q = 1.001$ at the magnetic axis to $q = 1.011$ at the plasma edge. The resistive wall is constructed to follow the constant-μ contour of the (μ, θ) confocal-ellipsoidal coordinate system defined in the article by Dobrott and Chang [18]. The analytically calculated

normalized growth rate must be multiplied by the normalized Alfvén frequency to compare with the actual growth rate calculated numerically.

We calculate the growth rate analytically and numerically for several equilibria with elongations ranging from $\kappa = 1.2$ to $\kappa = 2.0$. The numerical growth rates are calculated as described in the previous section. We do not need to do the convergence in the ψ_{rat} parameter discussed in Section 3 because we are using a fixed-boundary, non-separatrix equilibrium. The numerical calculation presented here used 50 radial finite elements, 128 Θ-points around the circumference, a total of 31 poloidal harmonics from -15 to $+15$, and 50 radial surfaces in the equilibrium calculation. The analytic growth rates are calculated from the dispersion relation (48) and renormalized as discussed above. The results of this comparison are shown in Fig. 2a. The comparison is excellent for the range of elongations tested here.

We also compare the growth rates calculated by both methods with no surrounding resistive wall. The analytic growth rates are given by Eq. (49). The results for the case with no resistive wall are presented in Fig. 2b for the same range of elongations. In this case as well, we see an excellent comparison between the numerical results and those predicted by the analytic model.

4.1.3. Numerical Convergence Properties

It is important to demonstrate the convergence properties of the code with respect to the numerical parameters used in the calculation. We consider first the convergence properties with respect to the total number of poloidal harmonics M defining ξ_ψ in Eq. (29).

The theory of spectral methods [36, 37] tells us that with a Fourier series expansion one can expect the kth coefficient of the expansion to decay faster than any inverse power of

k (exponential convergence) when the function and all its derivatives are infinitely smooth and periodic. There must be enough terms in the expansion to represent all the structure of the function, but beyond that one should see an exponential convergence, also termed "spectral accuracy."

In a problem in which such infinite smoothness is not present, but some sort of discontinuity exists, one no longer sees exponential convergence, but rather one obtains a global convergence of order $1/M^2$. We shall see this behavior in the next section when we consider equilibria with separatrices.

In the case of the simple large-aspect-ratio elliptical equilibrium, the smoothness and periodicity constraints are satisfied, and in fact we see a definite exponential convergence in the poloidal harmonics in Fig. 3. Furthermore, the analytic theory of Rutherford [8] tells us that only the odd-m harmonics contribute to the unstable eigenfunction, and in fact we see only odd-m contributions to the eigenfunction. Furthermore, there is absolutely no change in the eigenvalue when the calculation is performed with m_{odd} harmonics or with $m_{\text{odd}} + 1$ harmonics.

4.2. Code Test: Realistic Numerical Model

In this section we perform a vertical stability calculation for a CIT equilibrium with a surrounding resistive vacuum vessel wall. We shall compare our results with those obtained using the TSC [25]. Vertical instability growth rates are calculated using TSC by perturbing an up–down symmetric equilibrium and then tracking the vertical motion of the plasma by observing the time development of the flux difference between pairs of up–down symmetric flux observation points. Several pairs are typically used. These flux differences are fit to an exponential to obtain a growth rate.
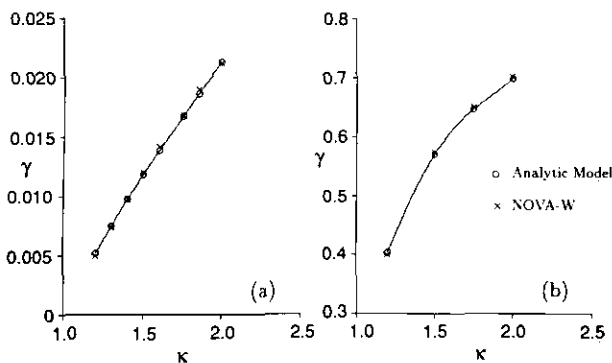

FIG. 2. (a) Comparison of resistive wall growth rates γ from the NOVA-W code to those of the analytic model with respect to ellipticity κ of the plasma. The growth rates γ are normalized here to correspond to the analytic model. For these model equilibria we have $B_T = 1$, $q_{\text{edge}} = 1.011$, and $X_{\text{mag}} = 10$. (b) Comparison of growth rates γ from the NOVA-W code with those of the analytic model with respect to ellipticity κ of the plasma. This is for the case of a plasma with no wall.
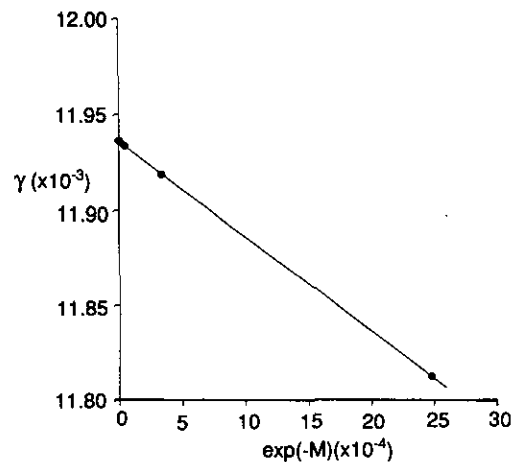

FIG. 3. Growth rate convergence in Fourier harmonics for the elliptical plasma $\kappa = 1.5$ equilibrium. Note the exponential convergence in the poloidal harmonics for this simple equilibrium.

In order to obtain an accurate growth rate by this method, one must do a convergence in the mass-enhancement factor (FFAC) that is used by TSC [25] to compensate for the difference between the resistive and ideal MHD time scales. The factor FFAC corresponds to the factor by which the Alfvén time scale is artificially slowed down in the TSC calculation. This corresponds to increasing the magnitude of the ion mass by a factor of $FFAC^2$. Several runs must be performed at different values of FFAC, and an extrapolation to $FFAC = 1$ is made to get a converged growth rate. The run time of each TSC simulation is proportional to $1/FFAC$ and, although accurate growth rates are obtained, the method is computationally expensive. In addition, TSC advances the *nonlinear* MHD transport equations in time; thus calculating the *linear* growth rates can be difficult if the arbitrary initial perturbation (which is clearly not the true eigenfunction) produces transients that are slow to decay. One can calculate the linear growth rate only after these transients have died away. However, if these transients decay slowly, then the displacement may become large and introduce new nonlinearities.

The CIT equilibrium used here is a $\kappa = 2$ (at the 95 % flux surface) diverted plasma with relatively low triangularity ($\delta = 0.26$), which is in the current-ramp stage (just prior to flat-top) of the CIT evolution. The parameters describing the CIT equilibrium are given in Table I. The CIT vacuum vessel structure consists of Inconel 625 (resistivity $\eta = 1.35 \times 10^{-6}\Omega$-m) on the inboard region and Inconel 600 ($\eta = 1.08 \times 10^{-6}\Omega$-m) on the outboard region. The thickness varies from 4 cm on the inboard region to 8.75 cm on the thickest outboard section. The wall definition was entered using the same points defining the vacuum vessel wall as in the TSC calculation. It is specified to have the same total resistance as the sum of all the conductors that make up the wall in the TSC calculation.

The resistive wall contour used in the NOVA-W calculation is shown in Fig. 4. The Θ-grid is shown connecting the wall to the plasma surface. Note also that the direction of increasing Θ is clockwise in this coordinate system.

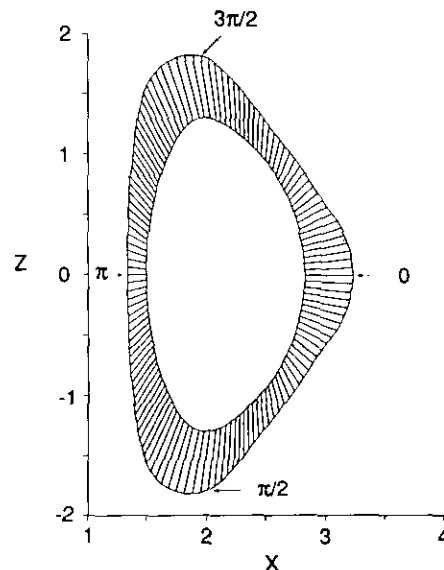The NOVA-W growth rate is calculated following the

FIG. 4. CIT wall contour used in the NOVA-W calculation. The points of the Θ-grid are shown on the wall and plasma surfaces, and the corresponding points are connected with line segments to show the relation between the wall points and the points on the plasma surface. The points designated by $\Theta = 0$, $\pi/2$, π, $3\pi/2$ are indicated on the figure.

numerical procedure outlined in Section 3. The CIT equilibrium has a separatrix surface, and we must therefore perform a convergence study as discussed in Section 3. The convergence of the growth rate γ as a function of ψ_{rat} is shown in Fig. 5. We obtain the converged growth rate of $\gamma = 80.31 \text{ s}^{-1}$ ($\tau = 12.45$ ms). This compares well with the result obtained from TSC, $\gamma = 80.65 \text{ s}^{-1}$ ($\tau = 12.4$ ms).

Now consider the convergence of the growth rate in poloidal harmonics for the CIT ($\psi_{rat} = 0.95$) equilibrium. Following the discussion in Section 4.1.2 regarding the convergence properties of the spectral method, we do not expect an exponential convergence in this case, because of discontinuities in derivatives of some of the equilibrium
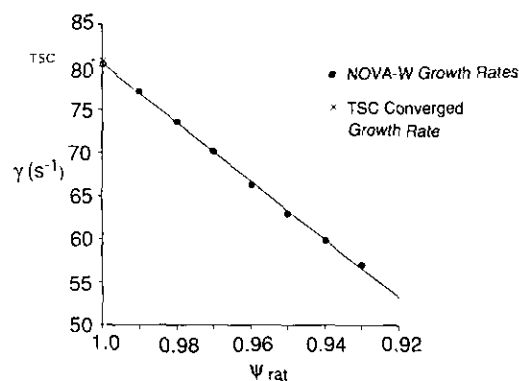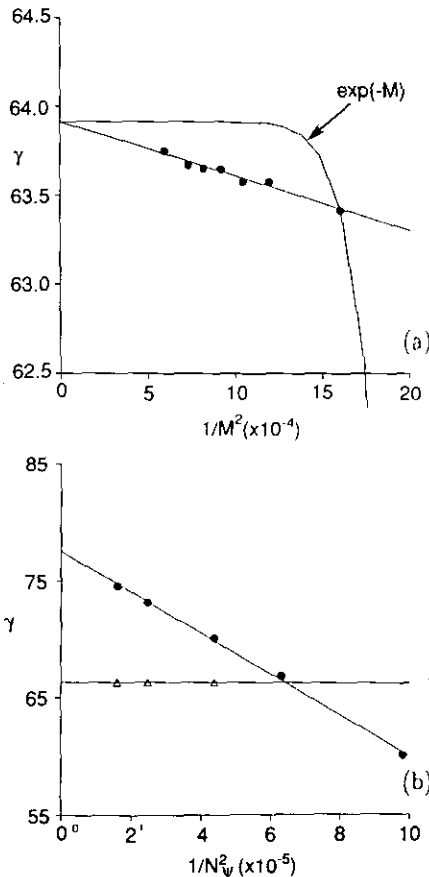
TABLE I

Equilibrium Parameters of CIT Plasma Used in the Passive Stabilization Study

Plasma current I_p	12.30 MA
Major radius R_0	2.182 m
Minor radius a	0.660 m
Elongation $\kappa(95\%)$	1.996
Triangularity $\delta(95\%)$	0.258
Toroidal field $B_T(0)$	11.0 T
$q(95\%)$	4.5
β	0.0092
$n_e(0)$	$1.08 \times 10^{21} \text{ m}^{-3}$

FIG. 5. Convergence of NOVA-W growth rates with respect to ψ_{rat}. Also shown is the converged value of the TSC calculated growth rate. The comparison is seen to be quite good.
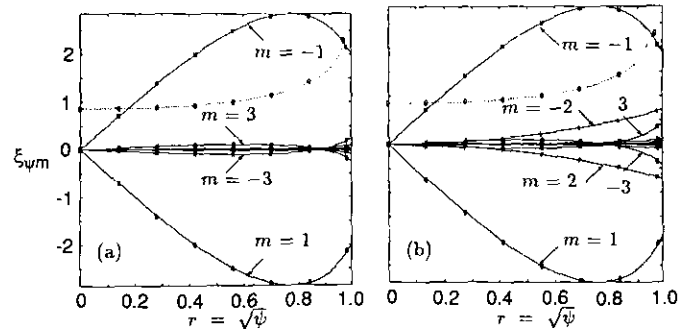
metric quantities at the plasma boundary due to the exist-
ence of an x-point. In fact, the results shown in Fig. 6a
indicate a $1/M^2$ convergence for this equilibrium.

In Fig. 6b we see the convergence of the growth rate γ
with respect to the number of radial surfaces N_ψ needed to
resolve the equilibrium. Whereas for the $\psi_{rat} = 0.96$ equi-
librium we see that there are sufficient surfaces ($N_\psi > 100$)
to obtain a converged growth rate, the growth rate for the
$\psi_{rat} = 0.99$ equilibrium keeps increasing with larger N_ψ.
Therefore one must perform a convergence in N_ψ for the
larger ψ_{rat} equilibrium.

Figure 7a shows the Fourier modes of the displacement
eigenfunction ξ_ψ for the CIT equilibrium used in this study.
Figure 7b shows ξ_ψ for a uniform vertical rigid shift of the
CIT equilibrium. It is clear that these two forms of ξ_ψ are
quite different, and therefore the true eigenfunction differs
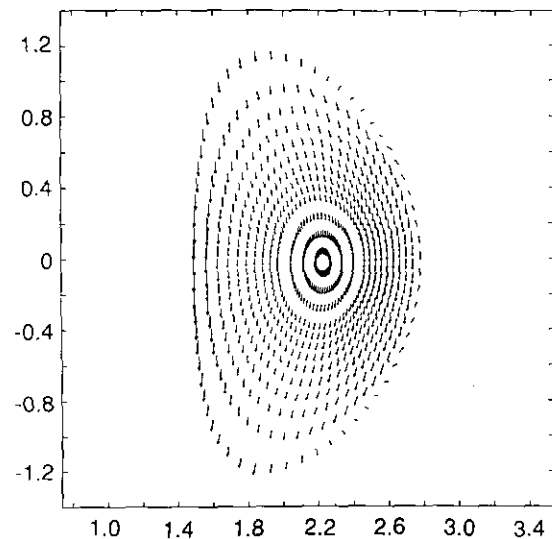significantly from a rigid vertical shift. In particular, the

FIG. 7. (a) Fourier components of the radial displacement of the
eigenfunction ξ_ψ vs. $\sqrt{\psi}$ for the CIT ($\psi_{rat} = 0.95$) equilibrium. The eigen-
function is dominated by the $m = \pm 1$ components. There is also a small
contribution from the $m = \pm 3$ components, which have considerable
variation in structure as a function of r. (b) Fourier components of a
uniform rigid shift. The form of the $m = 2, 3$ components is clearly much
different from that of the true eigenfunction.

$m = 2, 3$ components are nearly zero for the true eigenfunc-
tion, whereas there are significant $m = 2, 3$ components
needed to represent the rigid shift for this equilibrium.

Figure 8 shows the projection of the displacement ξ onto
the poloidal plane and indicates the motion of the unstable
plasma. We can see how it differs from a vertical shift. The
plasma displacement has a significant radial component
superimposed on the vertical motion. The consequence is
that the unstable plasma motion is toward the x-point in the
lower half-plane. It is clear from Figs. 7 and 8, therefore,
that the unstable motion of the CIT equilibrium is not

FIG. 6. (a) Growth rate convergence in Fourier harmonics for the
CIT ($\psi_{rat} = 0.95$) equilibrium. The results show a $1/M^2$ convergence for
this equilibrium. A curve defining an $\exp(-M)$ convergence is drawn
from the converged value through the rightmost point for comparison.
(b) Growth rate convergence in the number of equilibrium surfaces N_ψ^2 for
the $\psi_{rat} = 0.99$ (circles) and $\psi_{rat} = 0.96$ (triangles) equilibria. Note that for
this number of surfaces ($N_\psi > 150$) the $\psi_{rat} = 0.96$ is well converged, while
the $\psi_{rat} = 0.99$ equilibrium requires a far greater number of surfaces in the
equilibrium calculation to obtain convergence.

FIG. 8. This plot shows the instability displacement vectors for the
CIT equilibrium. Note how the displacement varies from a rigid vertical
shift. The true eigenfunction appears to be primarily vertical, but with some
inward motion (toward the symmetry axis) superimposed. The overall
effect is that the motion is in the direction of the x-point, or the "corner"
of the D-shaped plasma. This variation from the rigid vertical shift is shown
in terms of the Fourier components in Fig. 7.

particularly well represented by a uniform rigid shift. The NOVA-W code is ideally suited for examining the nonrigid aspects of the axisymmetric instability and how these nonrigid components can be affected by the feedback system. We have examined the non-rigid components of the eigenfunction and how they interact with the passive conductors and active feedback in more detail in another publication [38].

5. ACTIVE FEEDBACK RESULTS

The placement of the active feedback coils is clearly of great importance to the effectiveness of a feedback system. This has been examined in detail for the DIII-D tokamak experiment [30, 39]. We are also interested in the importance of the proper placement of the flux-loop detector positions on the effectiveness of the feedback system (for a given configuration of feedback coils) in stabilizing the plasma. Therefore, we perform a study in which the flux-loop observation pair, which is used to measure the plasma's position, is moved to different locations on the inside of the vacuum vessel wall. The plasma equilibrium and active feedback coils do not change in this study. We use the CIT equilibrium and vacuum vessel introduced in Section 4.2. Figure 9 shows the CIT plasma boundary, resistive wall, active coils, and the four locations for the flux-loop observation pairs used in this study. We choose this equilibrium as an example for these calculations because it is identical to the equilibrium used in a similar study using TSC. While it is not close to the ideal limit and, therefore, it is not overly

difficult to stabilize, it is an interesting and illustrative example.

Figure 10 shows the results of the active feedback system using flux measurements from the four flux-loop pair positions shown in Fig. 9. The growth rate is plotted against proportional gain for the positions and values of derivative gain as labeled. The curve labeled (a) shows the γ vs. α_g curve for flux-loop pair no. 1 located at $(X_o, Z_o) = (1.415, \pm 0.65)$. The derivative gain is $\beta_g/\alpha_g = 0.01$ s. This is clearly the most effective flux-loop pair considered here. Indeed, it corresponds to the most effective region for active feedback flux measurements in the TSC calculations performed for the same configuration [28].

Magnetic measurements (flux and magnetic field measurements) are used in experiments to determine plasma position on a fast time scale [30, 40]. The NOVA-W code allows a feedback system with an arbitrary number and configuration of flux-loops and poloidal magnetic field measurements in the feedback law. However, in our example, we use the most straightforward case of a simple difference of the perturbed flux between two observation points, or flux loops, symmetric about the midplane as a measure of the vertical position of the plasma. The perturbed poloidal flux is the difference between the total poloidal flux of the displaced equilibrium and the equilibrium poloidal flux, which is symmetric about the midplane for symmetric plasmas and conductor configurations. Therefore, the perturbed flux is essentially the asymmetric flux with respect to the midplane. This is com-
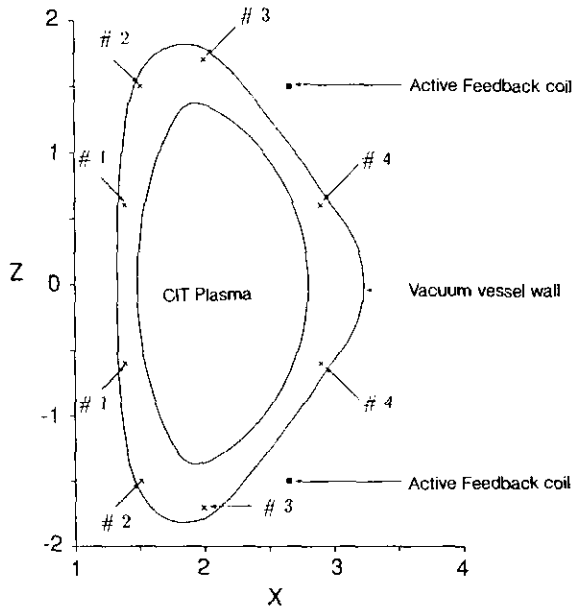

FIG. 9. CIT plasma boundary $(\psi_{rat} = 0.99)$, resistive wall, and locations of the flux-loop pairs.
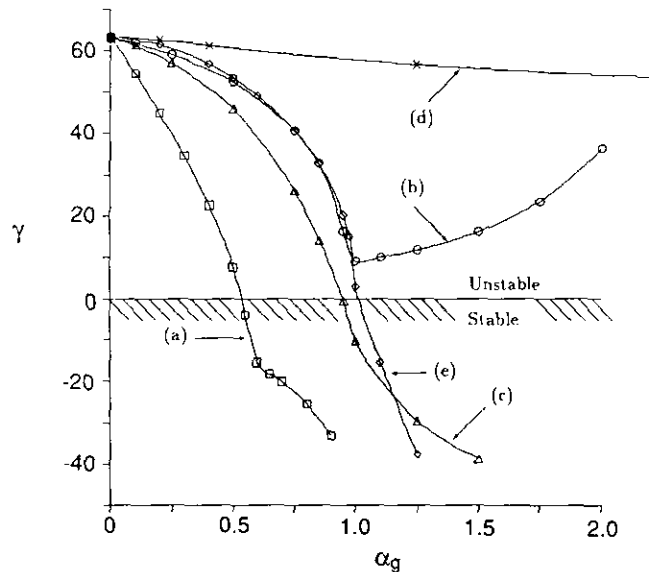

FIG. 10. Growth rates vs gain for various flux-loop locations on CIT. The flux-loop locations refer to the labels shown in Fig. 9: (a) squares, flux-loop position no. 1: $\beta_g/\alpha_g = 0.01$ s; (b) circles, flux-loop position no. 2: $\beta_g/\alpha_g = 0.01$ s; (c) triangles, flux-loop position no. 2: $\beta_g/\alpha_g = 0.02$ s; (d) crosses, flux-loop position no. 3: $\beta_g/\alpha_g = 0.02$ s; (e) diamonds, flux-loop position no. 4: $\beta_g/\alpha_g = 0.01$ s.

posed of three parts: the part due to the displaced plasma, the component from the currents in the feedback coils, and the part from the eddy currents in the passive conductors. An effective location is one that is sensitive to the perturbed flux contribution from the plasma with respect to a vertical displacement. Therefore a plot of perturbed flux contours in the vacuum region is a useful method for observing how effective a particular pair of flux loops is in determining plasma vertical position. From that we see how effective a pair of flux loops would be as part of the overall feedback system.

Figure 11 shows the perturbed flux contours in the vacuum region for the eigenfunction of the active feedback stabilization of the CIT equilibrium, with the normalized proportional gain $\alpha_g = 0.5$ (the gain is normalized to units of $2\pi/\mu_0$ amps/Weber-radians), using flux measurements at flux-loop position no. 1. One can see that these flux loops lie adjacent to perturbed plasma flux contours of relatively high flux. Figure 11 shows that the region including flux-loop position no. 1 and extending slightly higher along the inboard wall has the highest perturbed flux values and is therefore probably the best region in which to place the flux loops to detect vertical motion. The perturbed flux along the wall then decreases in magnitude as one moves the flux
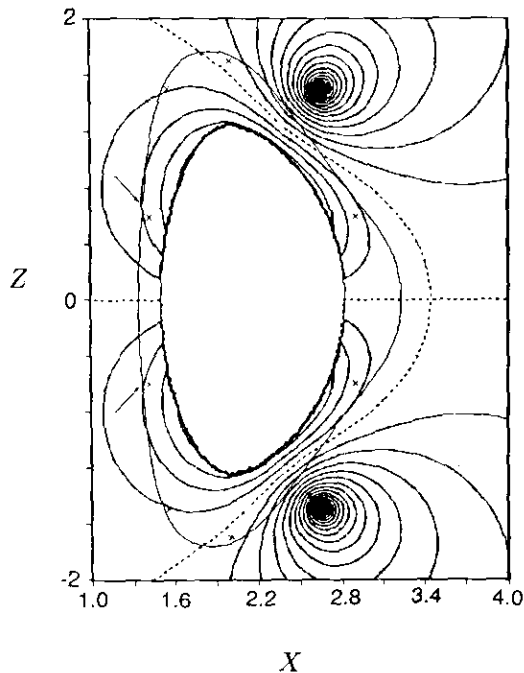
loops further from the midplane and toward the outboard side on the wall. One would expect, therefore, that by placing the flux loops at position no. 2 (see Fig. 9), the performance would be degraded somewhat, the reason being that the flux loops are now in a region with much smaller perturbed flux for a given vertical displacement. Therefore, the flux loops are less sensitive to the vertical motion of the plasma. These loops lie just outside the outermost (lowest magnitude) plasma flux contour, although they are still far from the zero-contour.

The curves marked (b) and (c) in Fig. 10 show the results for active feedback at flux-loop position no. 2, $(X_o, Z_o) = (1.51, \pm 1.50)$. Figure 12 shows these two curves apart from the other curves. Figure 12a shows γ vs. α_g, and Fig. 12b shows γ vs. the frequency of oscillation $|\omega_r|$. It is seen that the case with lower derivative gain $(\beta_g/\alpha_g = 0.01$ s) is always unstable. The growth rate decreases with increasing gain until a turning point is reached at $\alpha_g \approx 1.0$, at which point an increase in the gain no longer reduces the growth rate, but actually *increases* the growth rate at still higher gain. It is seen from Fig. 12 that at this turning point the value of $|\omega_r|$ increases rapidly from zero with increasing feedback gain. There is, therefore, an overshoot that begins approximately
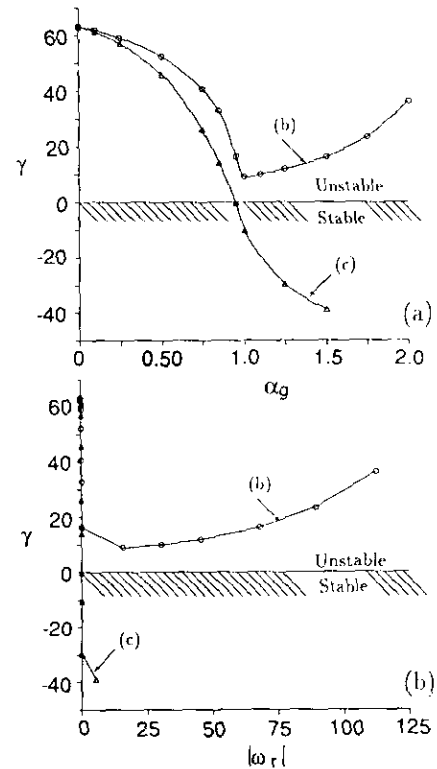

FIG. 11. Perturbed flux contours in the vacuum region of the CIT plasma ($\psi_{rat} = 0.95$) for active feedback in which the active feedback system uses flux measurements from flux-loop pair no. 1. The flux loops of pair no. 1 are represented by "x" symbols, which are indicated by the arrows. The zero-flux contour is shown as a dashed line. The flux contours increase in magnitude as one moves away from the zero-flux contour. The flux loops in this case lie on a contour of large plasma flux and are far from the zero-flux contour.

FIG. 12. (a) Growth rate γ vs. proportional gain α_g for the two cases using flux-loops at position no. 2. The circles correspond to the case with derivative gain $\beta_g/\alpha_g = 0.01$ s. The triangles correspond to $\beta_g/\alpha_g = 0.02$ s. (b) Growth rate γ vs oscillation frequency $|\omega_r|$ for the two cases with flux-loop pair no. 2. Doubling the derivative gain to $\beta_g/\alpha_g = 0.02$ s virtually eliminates the oscillation and stabilizes the plasma.

at the gain value at which there is a turning point in γ. In this case, once the gain value reaches a certain threshold, the feedback system drives this overshoot instead of reducing the growth rate. A further increase in gain increases the oscillation frequency caused by the overshoot and actually has the effect of increasing the growth rate as well.

The curve (c) shows the results of doubling the derivative gain to $\beta_g/\alpha_g = 0.02$ s. In this case we see that the growth rate continues to decrease smoothly and becomes stable. This case, with larger derivative gain, shows virtually no oscillation until well after the mode has been completely stabilized. The last point shows a small oscillation frequency with a large damping rate (negative growth rate) for the displacement. This is a good example of how increasing the derivative gain will reduce the oscillations and improve the overall performance of the feedback system. Lister et al. [30] showed the stability boundaries in gain space (β_g vs. α_g) for DIII-D. Their results show how the oscillations are reduced with increasing derivative gain, but that increasing the derivative gain too much has a destabilizing effect. The reduction in the efficacy of the feedback system as the flux loops are moved to a less sensitive position higher on the inboard wall from position no. 1 to position no. 2 agrees well with TSC results [28].

Curve (d) in Fig. 10 shows the results for active feedback with measurements taken at flux-loop position no. 3, $(X_o, Z_o) = (2.0, \pm 1.7)$. It can be seen that in this case the plasma is far from being stabilized, regardless of the value of the gain. There is only a small decrease in the growth rate with increasing gain. The curve shown is for $\beta_g/\alpha_g = 0.02$ s derivative gain, but the curve is nearly identical for $\beta_g/\alpha_g = 0.05$ s. In fact, the oscillation frequency $|\omega_r|$ for both cases is nearly zero. Therefore the problem in stabilizing the mode is not due to overshoot and oscillation, and increased derivative gain will not help. This agrees with results from TSC simulations [28] in which no gain combinations α_g, β_g were found that could come anywhere close to stabilizing the mode. Using this flux-loop location is apparently completely ineffective.

Figure 13 demonstrates the ineffectiveness of this flux-loop position in providing adequate feedback stabilization. The figure shows the perturbed flux contours for the active feedback using this pair of flux loops for $\alpha_g = 1$. It shows the contours of zero flux lying very close to the flux loops used for position measurement. The value of perturbed poloidal flux at these flux loops is very nearly zero. As the feedback gain is increased, the null contours move even closer to the flux loops, while the growth rate is only slightly reduced. Therefore these flux-loop locations are very insensitive to changes in the vertical position during active feedback.

It is the interaction of the perturbed plasma flux with the flux from the active feedback coils and the eddy currents in the passive conductors that creates this region of nearly zero flux. This effect demonstrates the importance of careful
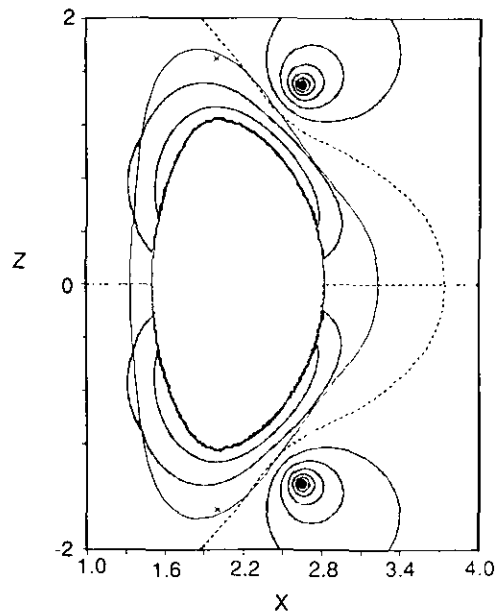

FIG. 13. Perturbed flux contours in the vacuum region for active feedback in which the active feedback system uses flux measurements from flux-loop pair no. 3. The flux loops of pair no. 3 are represented by "x" symbols, which are indicated by the arrows. The zero-flux contour is shown as a dashed line. The flux contours increase in magnitude as one moves away from the zero-flux contour. The flux loops in this case lie very close to the zero-flux contour.

placement of the flux loops taking into account the interaction of the active feedback system with the plasma flux and the passive conductors.

The inability of this flux-loop pair to stabilize the plasma is the result of the geometry of this particular configuration; it is not due to any significant deformation of the plasma. The important effect of the deformation of the plasma eigenfunction on the ability of a feedback system to stabilize the plasma has been examined in detail elsewhere [38].

If the active coil and passive conductor contributions to χ could be subtracted so that only the plasma contribution is measured, then any pair of up–down symmetric flux loops could effectively measure the vertical displacement and therefore control the plasma. The effects of the active feedback coils could be subtracted from the signal by redefining the perturbed flux measurement to be

$$\tilde{\chi}_o = \chi_o - \sum_i M_{o,i} I_i, \qquad (50)$$

where the sum is over the active feedback coils, and $M_{o,i}$ represents the coupling between the flux loop and the active feedback coil. The effects of the eddy currents in the vacuum vessel wall could, in principle, also be subtracted out. However, this would require a detailed knowledge of the eddy current distribution in the wall for the given plasma displacement and active feedback response. This could be

done in our calculation, but it might prove difficult in an experiment. Subtracting out only the active feedback coil contribution may improve the sensitivity of the flux loops, but it is not clear how much this would be improved without accounting for the eddy current effects—especially when the flux loops are inside the vacuum vessel wall.

Finally, curve (e) of Fig. 10 shows the results of using the flux loops at position no. 4 of Fig. 9, $(X_o, Z_o) = (2.9, \pm 0.6)$. This places the flux loops on the outboard side of the plasma at a relative position (with respect to the plasma) similar to that of the flux loops at position no. 1, but on the opposite side of the plasma. It is seen that the plasma can be stabilized using flux measurements at these points, although it takes a higher gain α_g than when using flux loops at position no. 1. Therefore, the position of this flux-loop pair is less sensitive than pair no. 1, but is still sensitive enough to successfully control the plasma. There is no need to increase the derivative gain beyond the 1% used in the first case.

Even though the flux loops at position no. 4 are almost as close to the active feedback coils as the flux loops at position no. 3, the geometry is such that the zero-flux contour does not closely approach the flux loops at position no. 4, as can be seen in Figs. 11 and 13. These loops lie within a region where the perturbed flux is large enough to provide a flux difference measurement that can stabilize the plasma. However, the region in which these flux loops lie has somewhat lower perturbed flux than that of flux-loop pair no. 1. Thus we would expect the feedback gain necessary for stabilization to be somewhat higher for flux-loop pair no. 4 than for pair no. 1; this is seen in Fig. 10. The ability of the active feedback to stabilize the plasma using these flux loops also agrees with TSC results [28].

6. DISCUSSION AND SUMMARY

We have developed a linear MHD stability code to examine the feedback stabilization of deformable tokamak plasmas by passive resistive conductors and active feedback currents in the vacuum region surrounding the plasma. This code, NOVA-W, is a modification of the linear, ideal MHD stability code NOVA.

The vacuum calculation has been modified to a formulation based on perturbed poloidal flux. This allows the representation of active feedback currents in the vacuum region, and the effects of eddy currents in the resistive wall can be represented by a jump condition in the normal derivative of the perturbed flux in accordance with a thin-wall approximation. The flux formulation also makes it straightforward to use magnetic measurements to represent the vertical displacement in agreement with experimental methods. A Green's function formulation relates the perturbed flux and the normal derivative of the flux on the plasma and resistive wall surfaces through a series of surface

integral equations. The boundary condition at the plasma–vacuum interface relates the perturbed pressure at the surface to the normal derivative of the flux. The perturbed flux is in turn related to the radial component of the instability displacement. This provides the necessary boundary condition for the solution of the linear MHD stability equations.

The code has been tested in the case of passive stabilization against an analytic model in the limit of an infinite aspect ratio for a simple elliptical plasma. The comparison is excellent. Another comparison is performed for a realistic tokamak configuration using the TSC. The comparison to the TSC results is excellent. The improved performance of NOVA-W over TSC allows one to obtain converged results using up to 10–20 times less computational time.

The NOVA-W code has been applied to the study of active feedback of the CIT tokamak design. The study focused on the comparison of effectiveness of the feedback system with regard to flux-loop location within the vacuum vessel. The results compare favorably to a similar study previously undertaken using the TSC code. It was seen that the sensitivity of the flux measurements varied with respect to the location at various points along the inside wall of the vacuum vessel. This greatly changes the efficacy of the feedback system. At some locations (e.g., flux loop pair no. 2) with an apparently reduced sensitivity of the flux measurements to plasma position, an increase in derivative gain can improve performance. At another location (flux loop pair no. 3) it was found that no combination of gains could stabilize the plasma; whereas other locations (such as flux loop pairs no. 1 and no. 4) allow effective feedback stabilization of the plasma.

APPENDIX A. ACTIVE FEEDBACK MATRIX DERIVATIONS

1. Case B: Detector Loops in Region II

In this case the observation points are outside the resistive wall. This region is bounded by only one surface (and extends to infinity). However, the feedback coil currents are in this region, so they make a direct contribution to the value of the perturbed flux at the observation points as well. Using the definition for the perturbed flux at a flux-loop position, Eq. (36), and the definition for the feedback currents, Eq. (14), we obtain for the perturbed flux at the observation points $\mathbf{r}_{o1}$ and $\mathbf{r}_{o2}$:

$$\chi(\mathbf{r}_{o1}) = f_1[-\mathbf{M}_{o1,w} \cdot \chi_w + \mathbf{G}_{o1,w} \cdot \nabla_n^+ \chi_w - S_1 \chi(\mathbf{r}_{o2})] \quad (A1)$$

$$\chi(\mathbf{r}_{o2}) = f_2[-\mathbf{M}_{o2,w} \cdot \chi_w + \mathbf{G}_{o1,w} \cdot \nabla_n^+ \chi_w + S_2 \chi(\mathbf{r}_{o1})], \quad (A2)$$

where $\mathbf{M}_{o1,w}$, $\mathbf{G}_{o1,w}$, and so on are defined as before and where

$$S_1 = \sum_m (\alpha_m - i\omega\beta_m)\, G(\mathbf{r}_{o1}; \mathbf{r}_c^m);$$

$$S_2 = \sum_m (\alpha_m - i\omega\beta_m)\, G(\mathbf{r}_{o2}; \mathbf{r}_c^m)$$
(A3)

$$f_1 = \frac{1}{(2 - S_1)}; \quad f_2 = \frac{1}{(2 + S_2)}.$$
(A4)

To solve for $\chi(\mathbf{r}_{o2})$ we substitute Eq. (A1) into Eq. (A2) to find

$$\chi(\mathbf{r}_{o2})[1 + S_1 S_2 f_1 f_2]$$
$$= f_2\{-\mathbf{M}_{o2,w}\cdot\chi_w^+ + \mathbf{G}_{o2,w}\cdot\nabla_n^+\chi_w$$
$$+ S_2 f_1[-\mathbf{M}_{o1,w}\cdot\chi_w^+ + \mathbf{G}_{o1,w}\cdot\nabla_n^+\chi_w]\}, \quad (A5)$$

and likewise for $\chi(\mathbf{r}_{o1})$ we obtain

$$\chi(\mathbf{r}_{o1})[1 + S_1 S_2 f_1 f_2]$$
$$= f_1\{-\mathbf{M}_{o1,w}\cdot\chi_w^+ + \mathbf{G}_{o1,w}\cdot\nabla_n^+\chi_w$$
$$- S_1 f_2[-\mathbf{M}_{o2,w}\cdot\chi_w^+ + \mathbf{G}_{o2,w}\cdot\nabla_n^+\chi_w]\}. \quad (A6)$$

These expressions are now substituted into Eq. (14) to give the expression defining the active feedback currents I_m:

$$I_m = \frac{(\alpha_m - i\omega\beta_m)}{F}\{-f_1(1 - f_2 S_2)\,\mathbf{M}_{o1,w}\cdot\chi_w$$
$$+ f_2(1 + f_1 S_1)\,\mathbf{M}_{o2,w}\cdot\chi_w$$
$$+ f_1(1 - f_2 S_2)\,\mathbf{G}_{o1,w}\cdot\nabla_n^+\chi_w$$
$$- f_2(1 + f_1 S_1)\,\mathbf{G}_{o2,w}\cdot\nabla_n^+\chi_w\}, \quad (A7)$$

where

$$F = 1 + S_1 S_2 f_1 f_2. \quad (A8)$$

Again we substitute this expression into the sum over the feedback coils in Eq. (36) to get our feedback equations. This defines the feedback matrices, and thus the elements (k, l) of $\mathbf{P}_w$ are defined by

$$\mathbf{P}_w^{k,l} = \frac{1 - K}{F} \sum_m (\alpha_m - i\omega\beta_m)\, G(\mathbf{r}_w^k; \mathbf{r}_c^m)$$
$$\times [-f_1(1 - f_2 S_2)\,\mathbf{M}_{o1,w}^l + f_2(1 + f_1 S_1)\,\mathbf{M}_{o2,w}^l], \quad (A9)$$

and the elements (k, l) of $\mathbf{N}_w$ are given by

$$\mathbf{N}_w^{k,l} = \frac{1}{F} \sum_m (\alpha_m - i\omega\beta_m)\, G(\mathbf{r}_w^k; \mathbf{r}_c^m)$$
$$\times [f_1(1 - f_2 S_2)\,\mathbf{G}_{o1,w}^l - f_2(1 + f_1 S_1)\,\mathbf{G}_{o2,w}^l], \quad (A10)$$

where K is the jump coefficient for the resistive wall as defined in Eq. (22). In this case $\mathbf{P}_p$ and $\mathbf{N}_p$ are identically zero because the plasma surface is in Region I, and therefore the plasma affects the perturbed flux at the observation points in Region II only through the boundary condition at the resistive wall.

The matrix equations (17)–(19) are again solved for $\nabla_n\chi_p$ in terms of χ_p. This case is a little more straightforward than the case presented in Section 2.3, because $\mathbf{P}_p$ and $\mathbf{N}_p$ are both identically zero. Therefore Eqs. (44)–(45) reduce to

$$\nabla_n\chi_p = \mathbf{E}^{-1}\cdot\mathbf{D}\cdot\chi_p, \quad (A11)$$

where

$$\mathbf{E} = \mathbf{G}_{pp} - \mathbf{C}\cdot\mathbf{B}^{-1}\cdot\mathbf{G}_{wp}$$
$$\mathbf{D} = (1 + \mathbf{M}_{pp}) - \mathbf{C}\cdot\mathbf{B}^{-1}\cdot\mathbf{M}_{wp}$$
$$\mathbf{C} = \mathbf{G}_{pw} + \mathbf{M}_{pw}\cdot\mathbf{A}^{-1}\cdot(\mathbf{G}_{ww} - \mathbf{N}_w) \quad (A12)$$
$$\mathbf{B} = \mathbf{G}_{ww} + (1 + \mathbf{M}_{ww})\cdot\mathbf{A}^{-1}\cdot(\mathbf{G}_{ww} - \mathbf{N}_w)$$
$$\mathbf{A} = (1 - \mathbf{M}_{ww} + K\mathbf{G}_{ww} - \mathbf{P}_w).$$

2. Feedback System Circuit Equations

In the previous cases we considered only the case of a "perfect" feedback system in which the feedback currents are a function only of the flux-loop measurements. In a realistic control system, of course, one would have the active feedback coils driven by a power supply, which is in turn controlled by the flux-loop measurements. The true dynamics of the current trajectories in the active feedback coils depend on the characteristics of the active feedback circuits. The currents are driven in the active feedback coils on the characteristic L/R time of the circuit, and there is coupling between the active feedback coils, between the coils and the vacuum vessel wall, and indeed between the coils and the plasma itself.

In order to make our model more realistic, we include the proper circuit equations in the feedback derivations and therefore in the feedback matrices. This has the additional benefit of accounting for the additional passive stabilization of discrete conducting elements in the vacuum region that are not part of the resistive wall. Therefore we will be able to include the passive effects of the active coils themselves or

whatever other conducting elements lie outside the vacuum vessel wall. We note that our model does not include power-supply characteristics such as a voltage limit or time-delayed response, however, as these do not fit within the framework of the simple linear model.

We define the voltage applied to a feedback coil to be some linear combination of the perturbed fluxes at prescribed observation points. We define the voltage to be proportional to the flux difference (and corresponding time derivative) between two observation points symmetric about the midplane. This is also analogous to the definition of the desired current for the ideal feedback-current model of Section 2.3. The feedback coil voltages are thus defined as

$$V_i = \tilde{\alpha}_i(\chi(\mathbf{r}_{o1}) - \chi(\mathbf{r}_{o2})) + \tilde{\beta}_i(\dot{\chi}(\mathbf{r}_{o1}) - \dot{\chi}(\mathbf{r}_{o2})). \quad \text{(A13)}$$

The new gain coefficient $\tilde{\alpha}$ and $\tilde{\beta}$ differ from the α and β of Eq. (14) and must satisfy the units of this equation. One simple definition would be to specify $\tilde{\alpha}_i$ and $\tilde{\beta}_i$ as simply the corresponding coil resistance r_i multiplied by the current gain coefficients α_i and β_i.

We are, of course, free to define V_i in any manner we choose. A more efficient feedback law is to define

$$V_i = V_g[I_i^{\text{want}} - I_i], \quad \text{(A14)}$$

where I_i^{want} is the feedback current we "want" in the coil, defined by Eq. (14), I_i is the actual coil current at that moment in time and V_g is the voltage gain coefficient.

We therefore have a circuit equation for the ith coil:

$$r_i I_i + L_i \frac{dI_i}{dt} + \sum_{j \neq i} M_{i,j} \frac{dI_j}{dt}$$
$$+ \sum_w M_{i,w} \frac{dI_v}{dt} + \frac{d}{dt}(M_{i,p} I_p) = V_i. \quad \text{(A15)}$$

This accounts for the resistance of the coil r_i, its self-inductance L_i, and its mutual inductance due to coupling with the other coils $M_{i,j}$, the resistive wall $M_{i,w}$, and the plasma $M_{i,p}$. The inductance terms can all be expressed in terms of the perturbed poloidal flux at the ith coil:

$$-\frac{d}{dt}\chi(\mathbf{r}_c^i) = L_i \frac{dI_i}{dt} + \sum_{j \neq i} M_{i,j} \frac{dI_j}{dt}$$
$$+ \sum_{v.v.} M_{i,v} \frac{dI_v}{dt} + \frac{d}{dt}(M_{i,p} I_p). \quad \text{(A16)}$$

Therefore the circuit equation (A15) becomes

$$r_i I_i = V_i - \frac{d}{dt}\chi(\mathbf{r}_c^i) = V_i + i\omega\chi(\mathbf{r}_c^i). \quad \text{(A17)}$$

We make use of the equation specifying the flux at an "observation point" in the vacuum region (this observation point is simply the position of the coil in Eq. (A16)), and we use the definition for V_i from Eq. (A13). Then the circuit equation for the ith coil is

$$(r_i - i\omega L_i)I_i - \frac{i}{2}\omega\mu_0 \sum_{j \neq i} G(\mathbf{r}_c^i; \mathbf{r}_c^j)I_j$$

$$= (\tilde{\alpha}_i - i\omega\tilde{\beta}_i)(\chi(\mathbf{r}_{o1}) - \chi(\mathbf{r}_{o2}))$$

$$+ \frac{i\omega\mu_0}{4\pi} \oint_{w+} \frac{dl_w}{X_w} (\hat{\mathbf{n}} \cdot \nabla G(\mathbf{r}_w; \mathbf{r}_{o1})) \chi(\mathbf{r}_w)$$

$$- \frac{i\omega\mu_0}{4\pi} \oint_{w+} \frac{dl_w}{X_w} G(\mathbf{r}_w; \mathbf{r}_{o1})(\hat{\mathbf{n}} \cdot \nabla\chi(\mathbf{r}_w)), \quad \text{(A18)}$$

where the mutual inductance between two coils, $M_{i,j}$, is just given by $\frac{1}{2}\mu_0 G(\mathbf{r}_c^i; \mathbf{r}_c^j)$ and where the self-inductance of a square coil of dimension Δx located at $\mathbf{r}_c^i = (X_i, Z_i)$ is given by [41]

$$L_i = \mu_0 X_i \left[\ln\left(\frac{8X_i}{\Delta x}\right) - \left(\frac{\pi}{2} - \frac{1}{2}\ln 2\right) \right] + O\left[\left(\frac{\Delta x}{2X}\right)^2\right]. \quad \text{(A19)}$$

When we sum this over all the coils we can rewrite the equations in a matrix form that emulates Ohm's circuit law,

$$\mathbf{R}_{i,j} \cdot \mathbf{I}_j = \mathbf{V}_i, \quad \text{(A20)}$$

where $\mathbf{R}$ is the impedance matrix, $\mathbf{I}$ is the array of feedback coil currents, and $\mathbf{V}$ is the array of "voltage" expressions. The latter contains all the Green's function surface integrals that come from Eq. (A18). The elements of the matrix $\mathbf{R}$ are given by

$$\mathbf{R}_{i,j} = (r_i - i\omega L_i)\delta_{i,j} - \frac{i}{2}\omega\mu_0 G(\mathbf{r}_c^i; \mathbf{r}_c^j)(1 - \delta_{i,j}), \quad \text{(A21)}$$

where $\delta_{i,j}$ is the Kronecker delta. The elements of $\mathbf{V}$ are defined by the right-hand side of Eq. (A18). The expressions derived in the previous section for the flux-loop measurements for a pair of detectors either inside or outside the resistive wall may be substituted into the expression for the elements $\mathbf{V}_i$. In order to determine the true feedback currents to be included in Eq. (36) so that we can derive the form of the feedback matrices, we invert the matrix $\mathbf{R}$ in Eq. (A20):

$$\mathbf{I}_j = (\mathbf{R}^{-1})_{j,i} \cdot \mathbf{V}_i. \quad \text{(A22)}$$

Using the results for the flux-loop detectors located in Region I, we derive the active feedback matrices with the circuit equations included, so that the elements (k, l) of $\mathbf{P}_p$, $\mathbf{P}_w$, $\mathbf{N}_p$, and $\mathbf{N}_w$ are defined by

$$\mathbf{P}_p^{k,l} = -\sum_j G(\mathbf{r}_w^k; \mathbf{r}_c^j) \sum_i (\mathbf{R}^{-1})_{i,j}$$
$$\times (\tilde{\alpha}_i - i\omega\tilde{\beta}_i)[\mathbf{M}_{o1,p}^l - \mathbf{M}_{o2,p}^l]. \quad (A23)$$

$$\mathbf{P}_w^{k,l} = -\sum_j G(\mathbf{r}_w^k; \mathbf{r}_c^j) \sum_i (\mathbf{R}^{-1})_{i,j}$$
$$\times (\tilde{\alpha}_i - i\omega\tilde{\beta}_i)[\mathbf{M}_{o1,w}^l - \mathbf{M}_{o2,w}^l]$$
$$- i\omega\mu_0 \sum_j G(\mathbf{r}_w^k; \mathbf{r}_c^j) \sum_i (\mathbf{R}^{-1})_{i,j} [\mathbf{M}_{i,w}^l - K\mathbf{G}_{i,w}^l],$$
$$(A24)$$

$$\mathbf{N}_p^{k,l} = \sum_j G(\mathbf{r}_w^k; \mathbf{r}_c^j) \sum_i (\mathbf{R}^{-1})_{i,j}$$
$$\times (\tilde{\alpha}_i - i\omega\tilde{\beta}_i)[\mathbf{G}_{o1,p}^l - \mathbf{G}_{o2,p}^l], \quad (A25)$$

$$\mathbf{N}_w^{k,l} = \sum_j G(\mathbf{r}_w^k; \mathbf{r}_c^j) \sum_i (\mathbf{R}^{-1})_{i,j}$$
$$\times (\tilde{\alpha}_i - i\omega\tilde{\beta}_i)[\mathbf{G}_{o1,w}^l - \mathbf{G}_{o2,w}^l]$$
$$+ i\omega\mu_0 \sum_j G(\mathbf{r}_w^k; \mathbf{r}_c^j) \sum_i (\mathbf{R}^{-1})_{i,j} \mathbf{G}_{i,w}^l. \quad (A26)$$

Equivalent forms for the feedback matrices with the flux-loop detectors in Region II are easily derived. The elements (k, l) of $\mathbf{P}_w$ are given by

$$\mathbf{P}_w^{k,l} = \frac{(1-K)}{F} \sum_j G(\mathbf{r}_w^k; \mathbf{r}_c^j) \sum_i (\mathbf{R}^{-1})_{i,j} (\tilde{\alpha}_i - i\omega\tilde{\beta}_i)$$
$$\cdot [-f_1(1 - f_2 S_2) \mathbf{M}_{o1,w}^l + f_2(1 + f_1 S_1) \mathbf{M}_{o2,w}^l]$$
$$- i\omega\mu_0 \sum_j G(\mathbf{r}_w^k; \mathbf{r}_c^j) \sum_i (\mathbf{R}^{-1})_{i,j} [\mathbf{M}_{i,w}^l - K\mathbf{G}_{i,w}^l],$$
$$(A27)$$

and the elements (k, l) of $\mathbf{N}_w$ are given by

$$\mathbf{N}_w^{k,l} = \frac{1}{F} \sum_j G(\mathbf{r}_w^k; \mathbf{r}_c^j) \sum_i (\mathbf{R}^{-1})_{i,j} (\tilde{\alpha}_i - i\omega\tilde{\beta}_i)$$
$$\cdot [f_1(1 - f_2 S_2) \mathbf{G}_{o1,w}^l - f_2(1 + f_1 S_1) \mathbf{G}_{o2,w}^l]$$
$$+ i\omega\mu_0 \sum_j G(\mathbf{r}_w^k; \mathbf{r}_c^j) \sum_i (\mathbf{R}^{-1})_{i,j} \mathbf{G}_{i,w}^l. \quad (A28)$$

The quantities f_1, f_2, S_1, S_2, F and the jump coefficient K are defined above. The matrices $M_{i,w}$ and $G_{i,w}$ are defined

in the same fashion as $M_{o1,w}$ and $G_{o1,w}$, except that the observation point is now the ith feedback coil:

$$\mathbf{M}_{i,w} \cdot \chi_w = -\frac{1}{4\pi} \oint_w \frac{dl_w}{X_w} (\hat{n} \cdot \nabla G(\mathbf{r}_w, \mathbf{r}_c^i)) \chi(\mathbf{r}_w) \quad (A29)$$

$$\mathbf{G}_{i,w} \cdot \nabla_n \chi_w = -\frac{1}{4\pi} \oint_w \frac{dl_w}{X_w} G(\mathbf{r}_w; \mathbf{r}_c^i)(\hat{n} \cdot \nabla\chi(\mathbf{r}_w)). \quad (A30)$$

ACKNOWLEDGMENTS

REFERENCES

1. C. Z. Cheng and M. S. Chance, *J. Comput. Phys.* **71**, 124 (1987).
2. F. Troyon, R. Gruber, H. Saurenmann, S. Semenzato, and S. Succi, *Plasma Phys. Controlled Fusion* **26**, 209 (1984).
3. R. J. Goldston, *Plasma Phys. Controlled Fusion* **26**, 87 (1984).
4. B. Coppi, R. Dagazian, and R. Gajewski, *Phys. Fluids* **15**, 2405 (1972).
5. T. Ohkawa and H. G. Voorhies, *Phys. Rev. Lett.* **22**, 1275 (1969).
6. M. S. Chance, S. C. Jardin, and T. H. Stix, *Phys. Rev. Lett.* **51**, 1963 (1983).
7. K. Bol *et al.*, *Phys. Rev. Lett.* **57**, 1891 (1986).
8. P. H. Rutherford, MATT Report 976, Plasma Physics Laboratory (Princeton University, Princeton, NJ 08543, 1973).
9. M. Okabayashi and G. Sheffield, *Nucl. Fusion* **14**, 263 (1974).
10. K. Lackner and A. B. MacMahon, *Nucl. Fusion* **14**, 575 (1974).
11. M. D. Rosen, *Phys. Fluids* **18**, 482 (1975).
12. F. A. Haas, *Nucl. Fusion* **15**, 407 (1975).
13. E. Rebhan and A. Salat, *Nucl. Fusion* **16**, 805 (1976).
14. E. Rebhan and A. Salat, *Nucl. Fusion* **17**, 251 (1977).
15. D. Lortz, *Plasma Phys. Controlled Fusion* **32**, 117 (1990).
16. T. Pfirsch and H. Tasso, *Nucl. Fusion* **11**, 259 (1971).
17. S. C. Jardin, *Phys. Fluids* **21**, 1851 (1978).
18. D. Dobrott and C. S. Chang, *Nucl. Fusion* **21**, 1573 (1981).
19. E. Rebhan and A. Salat, *Nucl. Fusion* **18**, 1431 (1978).
20. S. C. Jardin and D. A. Larrabee, *Nucl. Fusion* **22**, 1095 (1982).
21. J. A. Leuer, *Fusion Technol.* **15**, 489 (1989).
22. S. W. Haney and J. P. Freidberg, *Phys. Fluids B* **1**, 1637 (1989).
23. L. C. Bernard, D. Berger, R. Gruber, and F. Troyon, *Nucl. Fusion* **18**, 1331 (1978).
24. N. Pomphrey, S. C. Jardin, and D. J. Ward, *Nucl. Fusion* **29**, 465 (1989).
25. S. C. Jardin, N. Pomphrey, and J. DeLucia, *J. Comput. Phys.* **66**, 481 (1986).
26. R. C. Grimm, J. M. Greene, and J. L. Johnson, *Methods in Computational Physics*, Vol. 16 (Academic Press, New York, 1976), p. 253.
27. D. Berger, R. Gruber, and F. Troyon, paper C3, 2nd European Conf. on Computational Phys., Garching, 1976 (unpublished).
28. S. C. Jardin, M. G. Bell, J. L. Johnston, *et al.*, *Fusion Technol.* **21**, 1123 (1992).

29. M. Abramowitz and I. A. Stegun, *Handbook of Mathematical Functions* (Dover, New York, 1965).

30. J. B. Lister *et al.*, *Nucl. Fusion* **30**, 2349 (1990).

31. M. S. Chance *et al.*, in *Proceedings, 8th International Conference on Numerical Simulation of Plasmas, PC-5, Monterey, CA, 1978.*

32. R. Lüst and E. Martenson, *Z. Naturforsch.* **15**, 706 (1960).

33. J. P. Freidberg, *Ideal Magnetohydrodynamics* (Plenum, New York, 1987), p. 314.

34. W. H. Press, B. P. Flannery, S. A. Teukosky, and W. T. Vetterling, *Numerical Recipes: The Art of Scientific Computing* (Cambridge Univ. Press, Cambridge, 1986).

35. B. C. Kuo, *Automatic Control Systems*, 5th ed. (Prentice–Hall, Englewood Cliffs, NJ, 1987).

36. C. Canuto, M. Y. Hussaini, A. Quarteroni, and T. A. Zang, *Spectral Methods in Fluid Dynamics*, Series in Computational Physics (Springer-Verlag, New York, 1988).

37. C. A. J. Fletcher, *Computational Galerkin Methods*, Series in Computational Physics (Springer-Verlag, New York, 1984).

38. D. J. Ward and S. C. Jardin, *Nucl. Fusion* **32**, 973 (1992).

39. E. A. Lazarus, J. B. Lister, and G. H. Neilson, *Nucl. Fusion* **30**, 111 (1990).

40. R. E. Bell *et al.*, in *Fusion Engineering, Proceedings, 13th Symp. Knoxville, TN, 1989*, Vol. 1 (IEEE, New York, 1990), p. 467.

41. F. W. Grover, *Inductance Calculations: Working Formulas and Tables* (Dover, New York, 1946).